Applied Thermal Engineering 290 (2026) 129965

Contents lists available at ScienceDirect

Applied Thermal Engineering

journal homepage: www.elsevier.com/locate/apthermeng

Research Paper

Cryogenic hydrogen liquefaction by high-expanding supersonic nozzles: A numerical study

Masoud Sahami [a,b,*], Hojat Ghassemi [c], Angel Terziev [a,b], Kostadin Fikiin [a,b], Daniele Fiaschi [d], George Pitchurov [a,b]

[a] Faculty of Power Engineering and Power Machines, Technical University of Sofia, BG-1000 Sofia, Bulgaria
[b] European University of Technology, European Union
[c] School of Mechanical Engineering, Iran University of Science and Technology, Narmak, Tehran, Iran
[d] Department of Industrial Engineering, University of Florence, Florence, Via S. Marta 3, 50135, Italy

ARTICLE INFO

Keywords:
Hydrogen liquefaction
Supersonic separation
Cryogenic nucleation
Non-equilibrium condensation
Droplet growth

ABSTRACT

Supersonic separation is a promising alternative to traditional cryogenic cycles that use energy-intensive Joule-Thomson valves, as it can increase the liquefaction yield by more than three times in LNG production processes. This study investigates the potential of supersonic nozzles with high area ratios for efficient hydrogen liquefaction through non-equilibrium condensation under realistic operation conditions. A one-dimensional CFD approach is employed to model the condensation process under cryogenic and high-pressure conditions at the nozzle inlet. To accurately characterize cryogenic gas and droplet behavior, the Peng-Robinson equation of state is combined with a revised Gyarmathy growth model, incorporating the Clausius-Clapeyron relation. The results demonstrate that lowering the inlet temperature and increasing the inlet pressure of the nozzle significantly enhance liquefaction yield, achieving a maximum liquid phase production of 22% under hypersonic conditions. Analysis also reveals that hydrogen condensation is very sensitive to the inlet conditions, such that the liquefaction yield is twice as sensitive to inlet temperature as to inlet pressure. Notably, the high specific heat capacity of hydrogen enables the formation of micron-sized hydrogen droplets, which facilitates the separation process.

1. Introduction

The rising global energy demand, along with the imperative to mitigate climate change, has catalyzed a deep shift towards sustainable, green, and renewable energy resources. Among the rich arsenal of clean energy technologies, hydrogen has emerged as a particularly promising energy vector, offering zero carbon emissions upon combustion [1–5]. Therefore, it is predicted that the global hydrogen energy consumption will be multiplied several times by 2050 [6]. Liquid hydrogen has been used successfully for many years as a cryogenic fuel for launching aerospace vehicles, but it is still difficult for vehicular use because of the high energy cost to produce it at low temperatures (at about 20 K), and serious problems of handling and storage [7]. It is possible to produce hydrogen gas by means of water electrolysis, natural gas reforming, solar or wind energy processes as a renewable and high heat value fuel [8–10]. However, as hydrogen molecules are very small, the risk of leakage from containers is high. Therefore, effective storage and transportation of hydrogen remain essential challenges that must be adequately addressed to facilitate its widespread adoption [11,12]. Liquefaction, which significantly reduces the volume of hydrogen, represents an effective pathway to enable its efficient storage and transportation, thereby playing a central role in building a hydrogen-based economy [6]. The density of liquid hydrogen is approximately twice that of high-pressure compact hydrogen gas. Moreover, the high energy density, compact storage, and easy transportation make liquid hydrogen a suitable fuel choice for aerospace, petroleum refining, and maritime shipping [11,12]. However, hydrogen condensation occurs at relatively low cryogenic temperatures, which makes the liquefaction process challenging and energy-intensive.

Traditional hydrogen liquefaction methods, primarily dependent on turbo-expanders and Joule-Thomson (J-T) throttle valves, have been employed since the pioneering work of James Dewar in 1898 [13]. Furthermore, methods including turbo-expanders (e.g., in the Linde-Hampson cycle and Claude cryocooler cycles with nitrogen precooling) and methods without turbo-expanders (e.g., magnetic refrigeration

* Corresponding author at: Faculty of Power Engineering and Power Machines, Technical University of Sofia, BG-1000 Sofia, Bulgaria.
E-mail addresses: masoud.sahami@tu-sofia.bg, masoud.sahamy@gmail.com (M. Sahami), h_ghassemi@iust.ac.ir (H. Ghassemi), aterziev@tu-sofia.bg (A. Terziev), k.fikiin@tu-sofia.bg (K. Fikiin), daniele.fiaschi@unifi.it (D. Fiaschi), george@tu-sofia.bg (G. Pitchurov).

https://doi.org/10.1016/j.applthermaleng.2026.129965
Received 10 November 2025; Received in revised form 16 January 2026; Accepted 23 January 2026
Available online 26 January 2026

Nomenclature

A	Nozzle cross-section area, m^2
a, b	Peng-Robinson parameters, $m^5/(kg.s^2)$, m^3/kg
c_L	Liquefaction yield
C_p	Gas isobaric specific heat capacity, $J/(kg.K)$
C_v	Gas isochoric specific heat capacity, $J/(kg.K)$
d	Diameter of droplets, μm
D_H	Hydraulic diameter of the nozzle section, m
e	Specific internal energy of two-phase flow, J/kg
f	Friction factor of nozzle wall
$\overrightarrow{F}$	Vector of surface flux
g	Gravitational acceleration constant, m/s^2
G	Gibbs free energy, J
h	Specific enthalpy of two-phase flow, J/kg
h_{fg}	Latent heat of condensation per unit mass, J/kg
J	Nucleation rate, $1/(m^3.s)$
k_B	Boltzmann constant, $m^2.kg/(K.s^2)$
Kn	Knudsen number
L_c	Length of convergent section, m
$\bar{l}$	Length of free molecular mean path, m
m	Mass, kg
m_r	Mass of cluster, kg
M	Molar mass, kg/mole
Ma	Mach number
n, n_p	Total droplets or particle number density, 1/kg
N	Total number of control volumes
P	Static pressure, vapor pressure, Pa
P_s	Saturation pressure, Pa
P_v	Vapor pressure, Pa
Pr_G	Prandtl number for the gas
$\overrightarrow{Q}$	Conservative variable vector
$R, \overline{R}$	Gas constant, Universal gas constant, $J/(kg.K)$
$R(x)$	Nozzle section radius, mm
Re	Flow Reynolds number
r	Droplet or cluster radius, μm
$\overrightarrow{S}$	Source term vector
St	Stokes number
S_P	Supersaturation degree
T	Flow temperature, K
t	Time, s
u	Flow velocity, m/s
We	Weber number
x	Axial distance from nozzle inlet, cm
v, V	Specific volume, Volume, m^3/kg, m^3
Z	Compressibility factor

Greek letters

α_r	Heat transfer coefficient, $W/(m^2.K)$
ΔG	Gibbs free energy formation of clusters, J
Δt, Δx	Time step, element length, s, m
ϵ	Wall roughness height, mm
ε	Solution convergence criteria
ϕ	Void fraction
λ_G	Thermal conductivity, $W/(m.K)$
γ	Isentropic exponent of real gas
μ	Dynamic viscosity, Pa.s
ρ	Density of two-phase mixture, kg/m^3
σ	Surface tension, N/m
τ_w	Wall shear stress, N/m^2

Subscripts

1	One vapor molecule
a	Ambient
c	Critical
d, D	Droplet diameter, Channel diameter
e	Exit
eq	Equivalent
G, L	Gaseous phase, Liquid phase
i	Elements index
n	Time step index
nuc	Nucleation
r	Droplet
s	Saturation
th	Throat
v	Condensable vapor
0	Nozzle inlet, Ideal gas
t	Total
$\overline{u}$	Average of 'u'

Abbreviations

AUSM	Advection Upstream Splitting Method
C	Compressor
CFL	Courant-Friedrichs-Lewy number
CNT	Classical Nucleation Theory
CPS	Cyclone Phase Separator
CV	Control Volume
IWESP	International Wet Steam Experimental Project
EOS	Equation Of State
HEX	Heat Exchanger
EXP	Expander
J − T	Joule-Thomson
PS	Phase Separator

cycles) have been developed for the liquefaction of hydrogen [13–18]. Classical hydrogen liquefaction methods, such as the cycles of Linde and Claude, are inherently complex and costly. A major hurdle is the hydrogen's negative J-T coefficient at room temperature, which necessitates precooling to −48 °C by bulky and expensive heat exchangers. Furthermore, the isenthalpic expansion process, occurring rapidly and adiabatically through J-T valves, is irreversible [19]. During this process, the temperature drop is considerable to provide the necessary low temperatures for intense hydrogen liquefaction. In Claude cycles, turboexpanders are normally used with the J-T valves to increase the efficiency of the refrigeration system by isentropic expansion and to extract power for compressors in the cycle. Erosion of the blades may also occur due to the presence of liquid droplets in the final turboexpanders [20]. As is known, hydrogen is highly flammable and can be ignited by sparks, static electricity, or rapid release of gas, thereby requiring the strictest possible control of cryogenic equipment to prevent explosion accidents. In this context, reducing moving parts is a desirable trend. Moreover, high friction and turbulence within the J-T valves dissipate energy and prevent the recovery of useful expansion work. This leads to the need for a large number of expensive heat exchangers and turbo-expanders in the cryo-cooler multi-stage cycle.

The principal disadvantages of hydrogen liquefaction by traditional refrigeration and separation methods are low efficiency and high-pressure drop throughout the mechanical parts [21–24]. The expense

of machining the turbo-expanders is high; they have complex structures and require an extra cost for maintenance in a safe state. Additionally, the rotary components of these devices generate vibrations, which pose a risk of unstable operation and flammability for hydrogen. Therefore, such conventional approaches are characterized by significant problems, including high energy consumption, bulky infrastructure, risk of explosion, and inherent inefficiencies arising from high-speed rotation and sealing complexities [25–30]. The operational and maintenance costs, along with the safety concerns related to handling the low-temperature and high-pressure environments, pose substantial barriers to the hydrogen liquefaction practices [2,31].

To overcome the limitations of conventional liquefaction methods, research on alternative technologies is ongoing intensively. Supersonic expansion by means of Laval nozzles offers a promising path capable of achieving very low temperatures without the complexities of rotating machinery, thereby offering a more efficient and compact alternative to the traditional separation devices, specifically in the low-pressure stage of cryocooler-cycles [19,32]. The expansion process in these devices is isentropic, i.e., it occurs with minimal friction and low turbulence. As a result, the flow energy, converted into kinetic energy, can effectively be recovered, so that there is no need for a turbo-expander in the low-pressure stage of these systems (see Fig. 1). This leads to a significant temperature drop, often eliminating the need for large heat exchangers in the liquefaction cycle. Simultaneously, supersonic nozzles are more compact and have a simpler configuration. These devices offer lower operational costs and do not require chemical inhibitors. Studies have shown that their liquefaction yield is boosted up to three times as compared with traditional expansion devices in cryogenic systems [19,32,33]. As the flow expands in the divergent section of the nozzle, the resulting liquid droplets are thrown towards the walls by inertia, thus forming a liquid film that can be collected by a strategically placed collector. Supersonic nozzles provide advantages such as a compact design, lower pressure drop, and the elimination of moving parts, which make them a more efficient and cost-effective alternative to traditional liquefaction devices [34,35]. Due to the lower level of turbulence in the compressible flow, the inviscid flow assumption and 1D analysis are easily applicable to study the gas and liquid phase behavior in such nozzles.

Non-equilibrium condensation, where vapor is transformed to liquid or solid phase without reaching thermodynamic equilibrium, is well-studied in industrial applications (such as supersonic separators for natural gas processing, CO_2 capturing, LNG production, and fresh water production) [36–43]. However, despite some foundational work on hydrogen and helium [10,44–46], a clear thermodynamic analysis of hydrogen liquefaction in supersonic nozzles under realistic operating conditions is still lacking. Hydrogen's unique thermophysical properties, notably its extremely low critical temperature (32 K) and high compressibility, create substantial challenges for the numerical modeling of supersonic liquefaction and its experimental validation [8,47,48]. By the numerical methods, the effects of various parameters (e.g., inlet pressure, temperature, swirl effects, and nozzle geometry) on the condensation process of various vapors can be investigated by using commercial or programming codes [49–54]. It has been demonstrated that 1D modeling codes based on algebraic, differential, or computational methods have enough accuracy when modeling non-equilibrium condensation in the nozzles [49,55–57]. Accurate prediction of hydrogen's thermodynamic behavior in the high-pressure cryogenic environment of the nozzle's convergent section requires real gas equations of state (EOS) and refined condensation models [49,50,55]. The scarcity of experimental data for hydrogen condensation in supersonic flows further emphasizes the need for robust numerical simulations to guide the design and optimization of these systems [45]. Simultaneously, the lack of data on the condensed hydrogen properties also challenges numerical studies.

Studies have shown that hydrogen liquefies in supersonic nozzles at very low temperatures [10,44–46]. However, these studies often employ impractical nozzle inlet conditions, such as pressures and temperatures near saturation (below 50 K). If such extreme conditions are obtainable, condensation can be achieved without needing a low-area-ratio nozzle for further reduction in temperature. Furthermore, due to computational costs and simulation limitations, previous research has not investigated the high-capacity liquefaction potential or the maximum yield achievable in high-expansion nozzles. These limitations originate from the steep slope of the hydrogen P-T saturation curve, which impacts the classical Gyarmathy droplet growth model and makes the non-equilibrium condensation problem highly sensitive to inlet conditions.

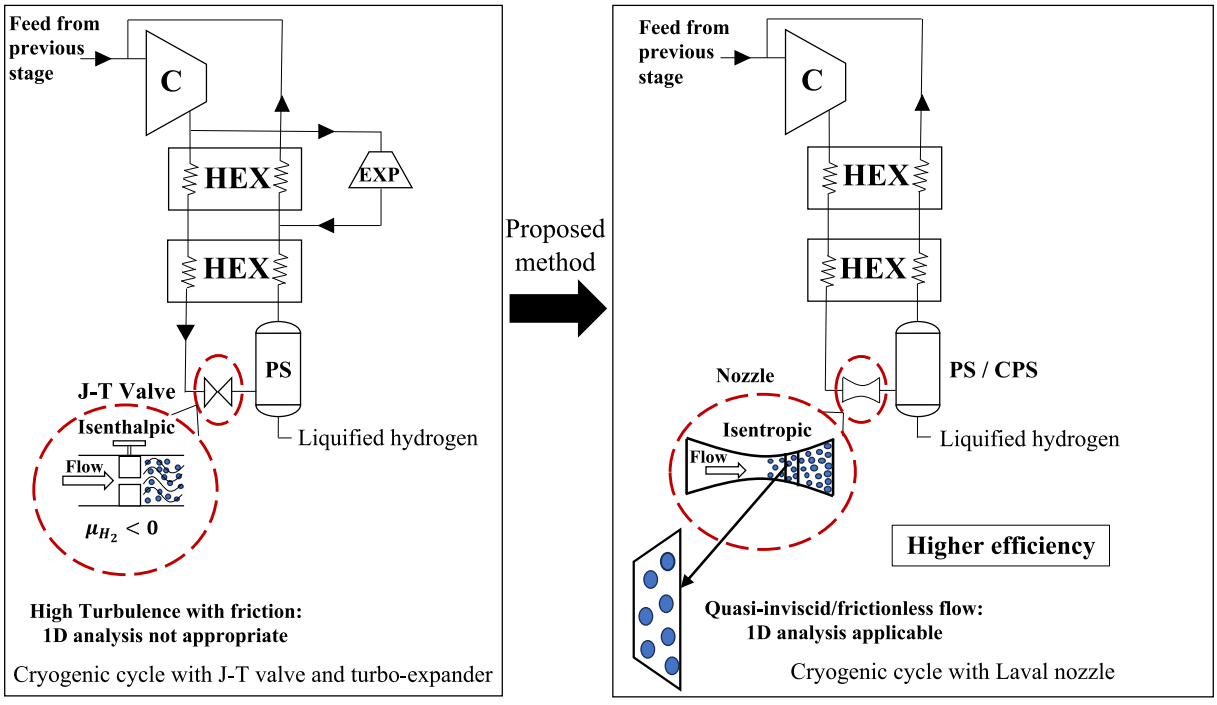

Fig. 1. Supersonic liquefaction as a substitution for classical cryogenic refrigeration cycles based on J-T valves and turbo-expanders.

Additionally, there is a conflict between the strong potential for droplets to grow and the very short time they spend through the hypersonic flow in the nozzle. Hence, there is an essential need to maximize the hydrogen condensation and to conduct the associated sensitivity studies. Achieving realistic hydrogen liquefaction requires initial cooling of the gas to approximately 100 K, readily attainable through industrial processes like Stirling cryocooling, liquid nitrogen precooling, heat exchanging, or even using exchangers that use the nozzle outflow to decrease its feed temperature (See Fig. 1) [58,59]. Subsequently, a high-compression ratio compressor increases the pressure, preparing the gas for condensation within the supersonic nozzle. Expansion through a high exit area ratio nozzle then provides the necessary low temperature conditions for maximum hydrogen liquefaction. The high specific heat capacity of hydrogen, alongside its low molecular mass, increases its droplet potential to grow more and reach large sizes, thereby facilitating the supersonic separation process and offering a pathway to future high-efficiency liquefaction technologies.

The present study addresses the above challenges and limitations by investigating the feasibility of hydrogen liquefaction via non-equilibrium condensation in high-expansion Laval nozzles. To perform the analysis, an inviscid 1D CFD approach was chosen, along with the Peng-Robinson EOS and modified Gyarmathy growth model using Clausius-Clapeyron expression. These presumptions are deemed accurate enough for simulating cryogenic two-phase flows with high slope P-T saturation diagrams. Utilizing classical nucleation and a single-diameter droplet growth model, coupled with the AUSM flux splitting method for solving two-phase flow dynamics, this study explores the sensitivity of thermodynamic and liquefaction properties on the inlet pressure and temperature operation conditions. This approach balances computational efficiency with accuracy, enabling comprehensive parametric studies to optimize supersonic liquefaction systems. By demonstrating the feasibility of this method under practical conditions and addressing gaps in previous research, the present work aims to advance cost-effective hydrogen liquefaction technologies, contributing to the transition towards a hydrogen-based economy. The study reveals that high area ratio nozzles and elevated inlet pressures are essential for achieving hypersonic flows and cryogenic temperatures necessary for efficient hydrogen liquefaction (in terms of the increased nucleation rate and overall liquefaction yield with higher inlet pressures, despite a decrease in Wilson point supercooling). The results of this paper can be a substantial step towards developing the liquefaction technology of hydrogen based on supersonic expansion.

2. Two-phase flow mathematical models

The analysis in this study focuses on modeling a one-dimensional, compressible, and inviscid flow. The current 1D Eulerian solver is a computationally efficient approach to model and simulate the dominant axial flow variations and the fundamental non-equilibrium thermodynamics of condensation. While the 1D Eulerian solver efficiently predicts bulk axial parameters, it neglects multi-dimensional phenomena critical to phase-change kinetics. Specifically, wall-bounded viscous effects create radial temperature gradients that suppress condensation by decreasing the nucleation rate. Furthermore, multi-dimensional shock-boundary layer interactions can cause flow separation, distorting pressure profiles and broadening the nucleation zone. These effects typically result in a more polydisperse droplet size distribution than the uniform growth predicted by 1D analysis. However, 1D models reliably estimate bulk axial parameters except for the fine-scale, localized fluid dynamics of the flow. The governing equations for two-phase nucleating flow in the nozzle consist of conservation laws, equations of state, and models for droplet nucleation and growth. These equations for the 1D analysis are detailed in the following sections.

2.1. Conservation equations

A time-dependent solution to the nonlinear conservation equations is obtained within the Eulerian framework, and these equations are as follows [60]:

$$\frac{\partial \vec{Q}}{\partial t}+\frac{\partial \vec{F}}{\partial x}=\vec{S} \tag{1}$$

The components of the conserved quantities $\vec{Q}$, surface fluxes $\vec{F}$, and the source terms $\vec{S}$ vectors are represented through the following vector expressions [60]:

$$\vec{Q}=\begin{bmatrix}\rho\\ \rho u\\ \rho e_t\\ \rho c_L\\ \rho n\end{bmatrix}$$

$$\vec{F}=\begin{bmatrix}\rho u\\ \rho u^2+P\\ \rho e_t u+Pu\\ \rho c_L u\\ \rho n u\end{bmatrix} \tag{2}$$

$$\vec{S}=\begin{bmatrix}-\frac{\rho u}{A}\frac{dA}{dx}\\ -\frac{\rho u^2}{A}\frac{dA}{dx}-\frac{4\tau_w}{D_H}\\ -\frac{\rho h_t u}{A}\frac{dA}{dx}\\ \frac{4}{3}\pi\rho_L r_c^3 J+4\pi\rho\rho_L r^2 n\frac{dr}{dt}-\frac{\rho c_L u}{A}\frac{dA}{dx}\\ J-\frac{\rho n u}{A}\frac{dA}{dx}\end{bmatrix}$$

Since the droplets in these nucleating flows have sub-micron sizes, so that their Stokes number are smaller than one ($\mathrm{St_d}\ll 1$), a no-slip condition is assumed between the phases within the momentum equation. In Eq. (2), the wall shear stress (τ_w) is determined via the Colebrook formula, which relies on the friction factor $f(\epsilon, \mathrm{Re_D})$. The total specific internal energy of the two-phase mixture within each cell (e_t) is then defined by Eq. (3) as follows:

$$e_t=h_G-c_L h_{fg}-\frac{P}{\rho}+\frac{u^2}{2} \tag{3}$$

where h_{fg} is the latent heat of condensation per unit mass, and ρ is the two-phase flow density, which is related to the gas and liquid densities through the following equation:

$$\rho=\left(\frac{1-c_L}{\rho_G}+\frac{c_L}{\rho_L}\right)^{-1} \tag{4}$$

The second term on the right-hand side of Eq. (4) is negligible compared with the first one. By using Eq. (1), the flow parameters (i.e., density, velocity, temperature, etc.) are then calculated at each time step. For single-component flows, the liquefaction yield can be determined by evaluating the liquid mass fraction (c_L).

2.2. Real gas model

Accurate analysis of the condensation in the nozzle under very low temperatures, particularly at the high-pressure inlet, necessitates a real gas equation of state (EOS). Errors in inlet flow state calculations propagate downstream in the domain numerically and significantly impact results. The Peng-Robinson EOS, known for its simplicity, flexibility, and accurate gas property predictions, is well-suited for this application and can be written as follows [61]:

$$P = \frac{\rho_G RT}{1 - b\rho_G} - \frac{a\rho_G^2}{1 + 2b\rho_G - b^2\rho_G^2} \tag{5}$$

where a and b are the coefficients of the Peng-Robinson EOS.

2.3. Non-equilibrium condensation models

Within the Eulerian-Eulerian framework, nucleation and droplet growth models are concurrently implemented. These processes begin when the gas enters a supersaturated state. Homogeneous nucleation rates are calculated by using the classical nucleation theory (CNT), where the free energy of cluster formation is determined by the following formula:

$$\Delta G = -m_r RT\ln(S_P) + 4\pi r^2\sigma \tag{6}$$

Here, m_r represents the mass of a cluster with radius r. The critical cluster radius is determined by finding the maximum of the Gibbs free energy with respect to the cluster radius, which results in the following expression [62]:

$$r_c = \frac{2\sigma}{\rho_L RT\ln(S_P)} \tag{7}$$

The classical nucleation rate, as determined by Eq. (8), establishes the rate of volumetric number density of critical clusters formed when assuming the stagnant bulk of the flow [62].

$$J_{\text{class}} = \frac{\rho_v^2}{\rho_L}\sqrt{\frac{2\sigma}{\pi m_1^3}}\exp\left(-\frac{\Delta G_c}{k_B T}\right) \tag{8}$$

The classical nucleation rate, which depends on vapor density (ρ_v), liquid density (ρ_L), Boltzmann's constant (k_B), molecular mass (m_1), and the Gibbs free energy of critical cluster formation (ΔG_c), is then modified by using the Kantrowitz correction. This modification considers the temperature difference (non-isothermal effects) and heat transfer between the phases. It improves the accuracy of predicting the Wilson points, pressure, and droplet radius distribution for two-phase flows (containing H_2O, N_2, etc.) relative to other alternatives such as classical, Courtney, Hale, Girshick-Chiu, and Wölk-Strey nucleation models at various temperatures [60,63–66].

$$J_{\text{Kant}} = \frac{J_{\text{class}}}{1 + \frac{2(\gamma-1)}{(\gamma+1)}\frac{h_{fg}}{RT}\left(\frac{h_{fg}}{RT} - \frac{1}{2}\right)} \tag{9}$$

where h_{fg} is the latent heat of condensation, i.e., the energy released when vapor molecules settle down on the droplet during the condensation. The droplet growth rate is determined by calculating the energy exchange between the droplet and the surrounding gas. Employing the Gyarmathy approximation for one-way thermal coupling of gas and droplet temperature, the growth rate is calculated as follows [60,67]:

$$\frac{dr}{dt} = \frac{\alpha_r}{\rho_L h_{fg}}\left(1 - \frac{r_c}{r}\right)(T_s - T) \tag{10}$$

Gyarmathy's growth model provides more accurate predictions of two-phase flow parameters for different vapors under various temperatures as compared with other alternatives such as the Hertz-Knudsen, Spalding, and Fuchs-Sutugin models [60,68,69]. The convective heat transfer coefficient (α_r) in Eq. (10) describes the heat transfer between the droplet and the gas. The relationship between the saturation temperature and pressure is then determined by using the Clausius-Clapeyron equation as a new approximation to better determine the droplet growth for gases with a high slope of P-T diagrams by the following expression [60]:

$$T_s = \frac{h_{fg}T}{h_{fg} - RT\ln(S_p)} \tag{11}$$

By substituting Eq. (11) in Eq. (10), the droplet growth model also becomes a function of supersaturation, so that there is no need for special correlations to determine the saturation temperature. The difference $(T_s(P_v) - T)$ in Eq. (10) is defined as the gas supercooling [70]. Based on Gyarmathy's general model, the convective heat transfer coefficient, valid for various droplet Knudsen numbers, is given by a correlated expression to satisfy the continuum and free molecular regimes as follows [60,71]:

$$\alpha_r = \frac{\lambda_G}{r\left(1 + \frac{2\sqrt{8\pi}}{1.5\text{Pr}_G}\frac{\gamma}{\gamma+1}\text{Kn}_r\right)} \tag{12}$$

where λ_G is the gas thermal conductivity. The droplet Knudsen number (Kn_r) and the gas Prandtl number (Pr_G) are calculated by Eqs. (13) and (14), respectively:

$$\text{Kn}_r = \frac{\bar{l}}{2r} = \frac{1.5\eta_G\sqrt{RT}}{P} \tag{13}$$

$$\text{Pr}_G = \frac{C_p\mu_G}{\lambda_G} \tag{14}$$

where μ_G is the dynamic viscosity of the gas.

2.4. Thermophysical properties

Equations detailed in Appendix A were used to determine the physical and thermophysical properties of both gas and liquid phases, including surface tension, droplet density, latent heat, saturation temperature, viscosity, thermal conductivity, and specific heat capacity of normal hydrogen (Para-Ortho) as the gaseous phase.

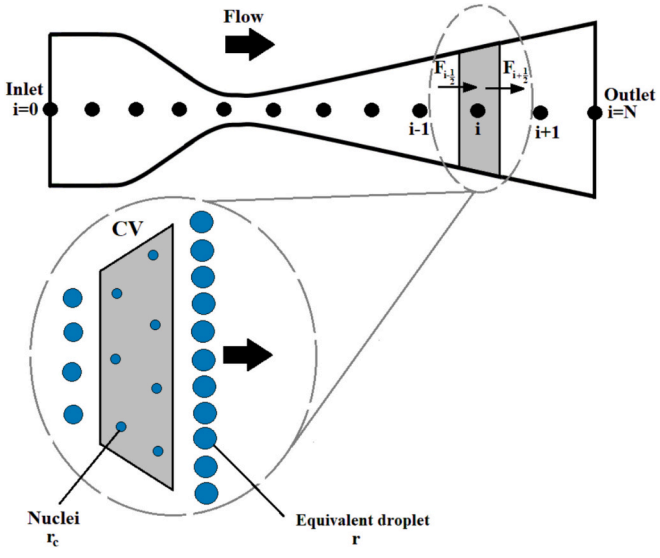

Fig. 2. Schematic of droplet growth and equivalent diameter at each nozzle control volume.

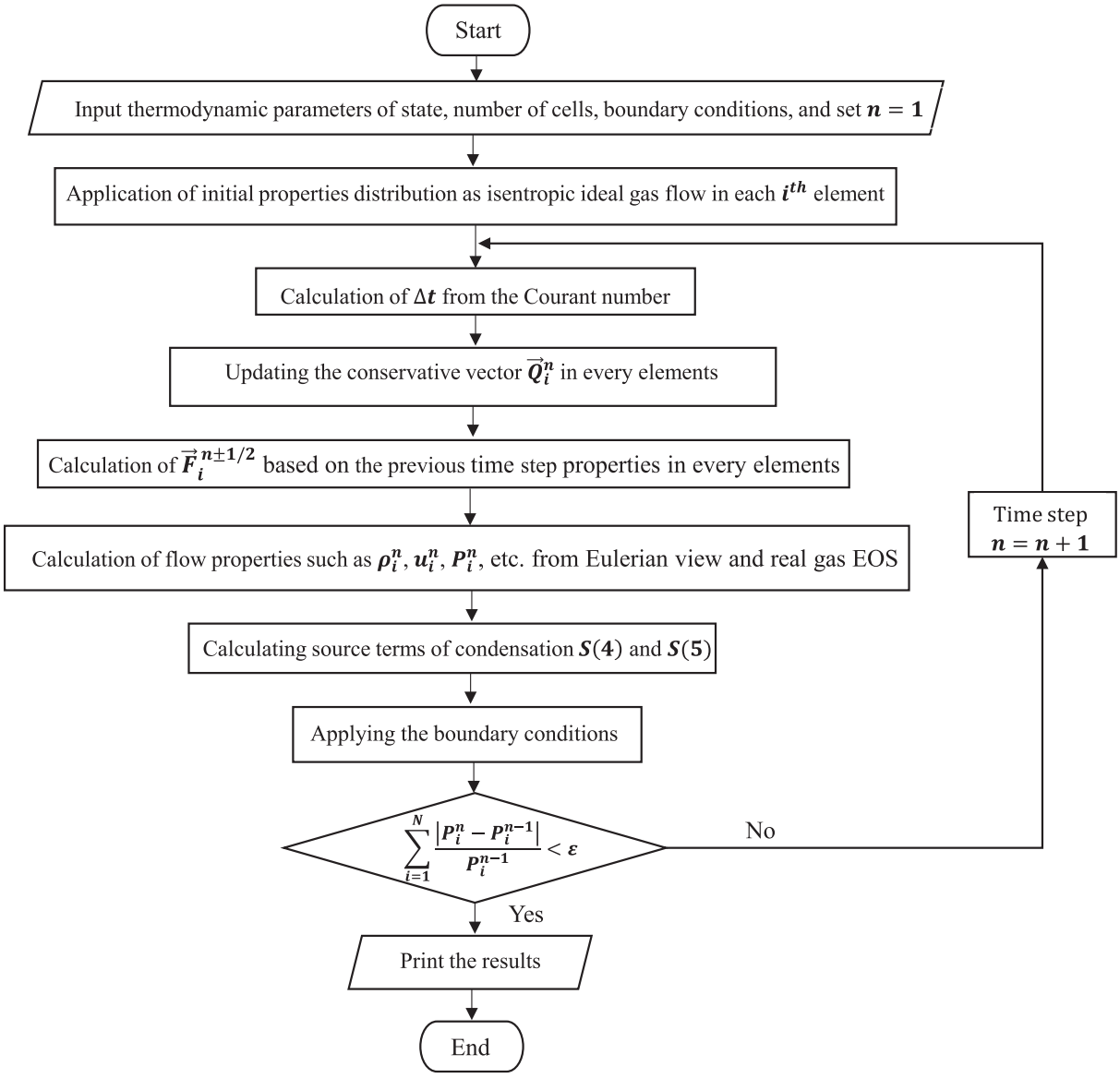

Fig. 3. Algorithm for analyzing the two-phase nucleating flows in the numerical model.

Table 1
Boundary conditions at the nozzle inlet and outlet.

Boundary condition	T	P	u	n	c_L
Inlet	T_0	P_0	$Q_0(2) = 2Q_1(2) - Q_2(2)$	0	0
Outlet			$\vec{Q}_N = 2\vec{Q}_{N-1} - \vec{Q}_{N-2}$		

2.5. Equivalent diameter of the droplets

The single-diameter approach serves as a primary engineering proxy for the liquefaction performance. In real separators, micron-sized droplets are sufficient for centrifugal separation and liquid film formation. Due to the small droplet size, the Weber number of droplets is low ($We_d < 12$) and droplet breakup is considered negligible [60]. Furthermore, the high-speed expansion creates a dilute dispersed phase with large void fractions ($\phi > 0.95$), where the short residence time makes coalescence negligible [60]. While a real polydisperse distribution exists, the predicted mean diameter can effectively approximate the feasibility of centrifugal separation in the nozzle. Thus, a single-diameter model,

Table 2
Main assumptions governing the model.

Assumption	Physical justifications	Range of validity
Inviscid 1D flow	Core flow dominates axial variations; high Reynolds number.	$Re_D > 10^5$
Flow continuity	The fluid behaves as a continuous medium.	$Kn_e \ll 1$
Homogeneous nucleation	Neglecting the impurities or foreign particles.	$n_p < 10^{12}$ m^{-3}
No-Slip condition for droplets	Small droplet relaxation time due to micro-scale size. Heat transfer between the phases follows the single motionless sphere convection with stagnant vapor.	$St_d \ll 1$
No coalescence for droplets	Dilute dispersed phase; high inter-droplet distance.	$\phi > 0.95$
No droplet breaking	Surface tension dominates aerodynamic drag.	$We_d < 12$
Single-diameter model	Uniform droplet size at each cross-section.	$\phi > 0.95$ and $We_d < 12$

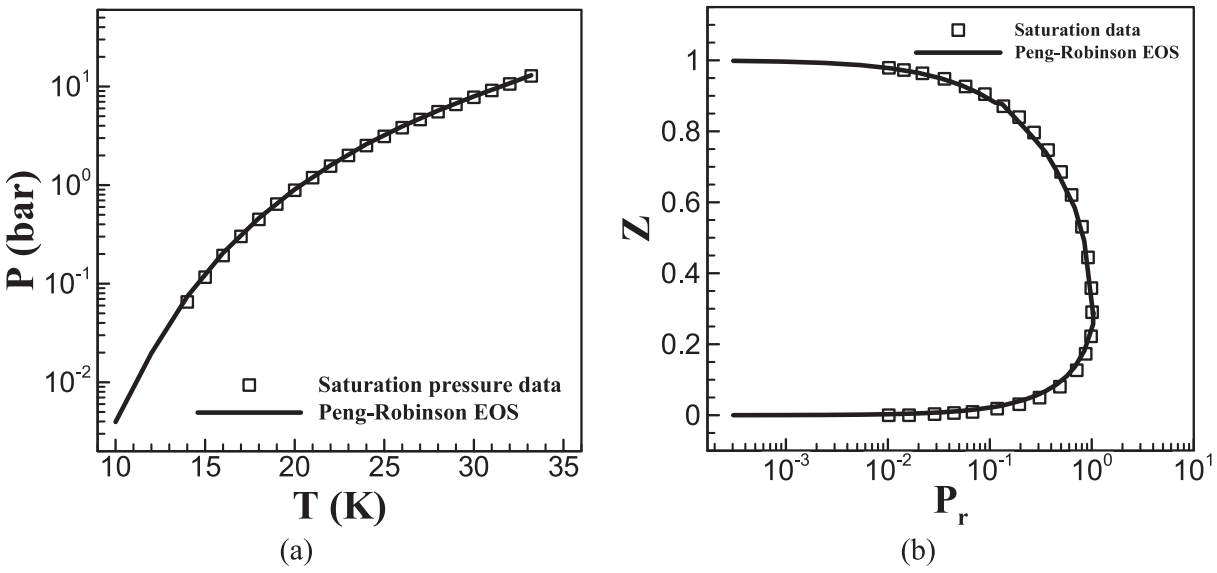

Fig. 4. Comparing hydrogen (a) saturation data and (b) compressibility factor with data available [73,74].

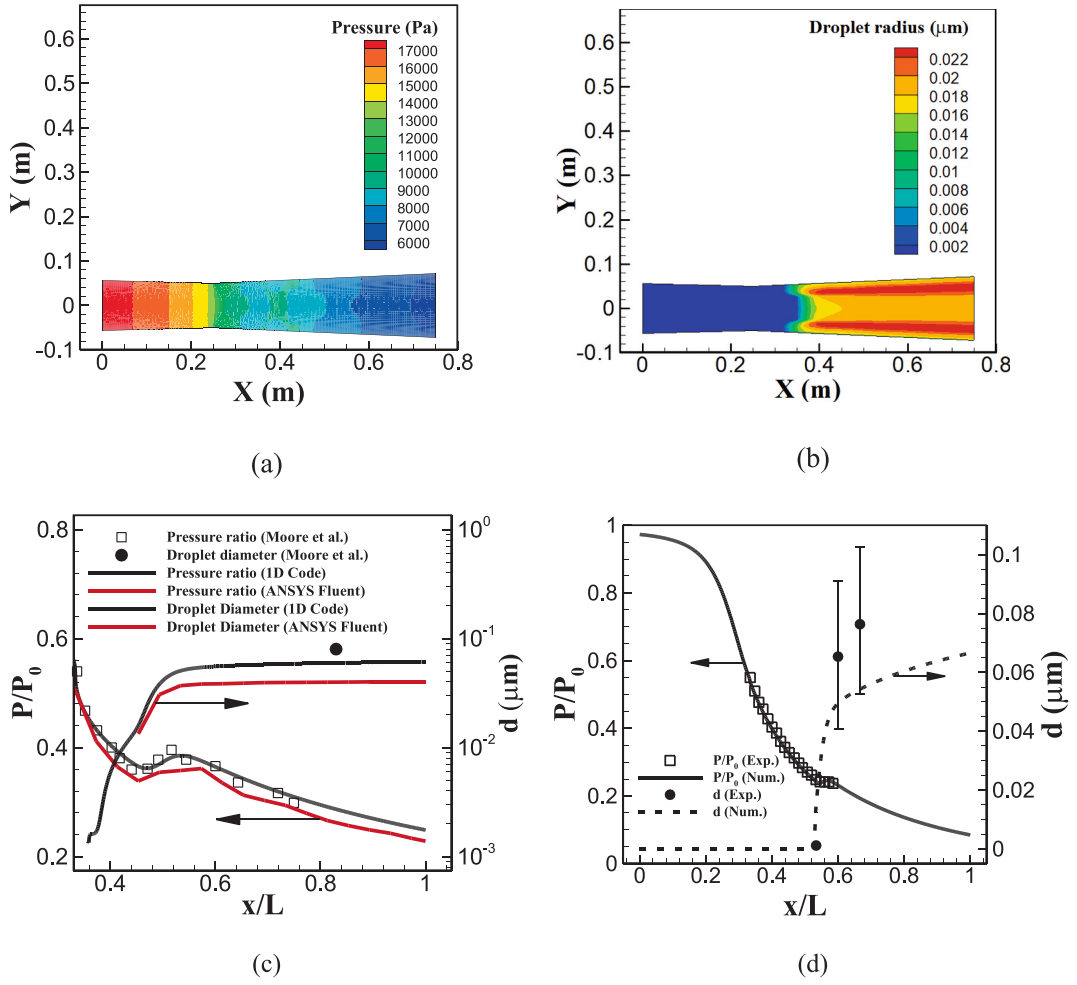

Fig. 5. Contours of (a) pressure and (b) droplet size distributions through the Moore nozzle using ANSYS Fluent. Comparing the pressure and droplet sizes resulting from the 1D model against experimental data and numerical solution of ANSYS Fluent at each section of: (c) Moore et al. data for water steam ($P_0 = 25$ kPa, $T_0 = 357.6$ K, $L = 750$ mm, and $\epsilon = 6.5 \times 10^{-4}$ mm) [75], and (d) IWSEP nozzle ($P_0 = 100$ kPa, $T_0 = 423.6$ K, $L = 133$ mm, and frictionless) [76].

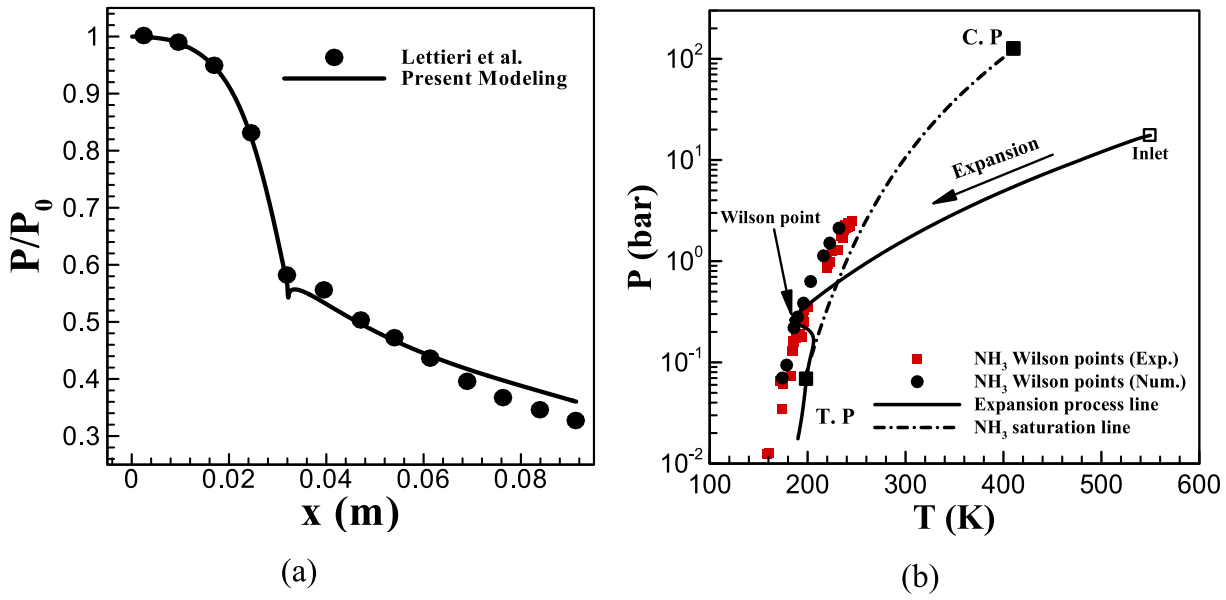

Fig. 6. Comparing the 1D modeling results against experimental data of: (a) pressure distribution in the nozzle of Lettieri et al. [77] for CO_2 ($P_0 = 95$ bar, $T_0 = 314$ K, $L = 91.5$ mm, and $\epsilon = 6.5 \times 10^{-4}$ mm), and (b) Wilson points reported by Jaeger et al. (frictionless) [78].

which serves as a primary indicator of the bulk liquefaction potential, is used to describe the droplet distribution in the domain. According to Fig. 2, each control volume contains two droplet groups: one originating upstream and growing, and another formed locally. Eq. (15) is used to calculate the equivalent diameter of these groups at each element.

$$r_{eq} = \frac{d}{2} = \sqrt[3]{\frac{6c_L}{\pi n \rho_L}} \tag{15}$$

where c_L is the liquid mass fraction, and n is the number density of all droplets.

2.6. Solution flowchart

The AUSM scheme is employed to solve the conservation equations. AUSM is well-suited for capturing shocks and steep gradients inherent in real gas flows. The computational domain is discretized into numerous control volumes, and the conservation equations are solved concurrently with droplet growth and nucleation models. The updated conservative vector is determined by calculating surface flux terms $\vec{F}^{n}_{i\pm\frac{1}{2}}$ and utilizing the previous time step's vector as follows [72]:

$$\vec{Q}_i^{n+1} = \vec{Q}_i^{n} - \frac{\Delta t}{\Delta x}\left(\vec{F}^{n}_{i+\frac{1}{2}} - \vec{F}^{n}_{i-\frac{1}{2}}\right) + \vec{S}_i^{n}\Delta t \tag{16}$$

At each time step, two independent parameters of state (such as pressure and temperature) are updated. The Peng-Robinson EOS is used to calculate the gas pressure, and subsequent parameters are derived from these updated values. Nucleation and droplet growth source terms ($S(4)$ and $S(5)$) are non-zero when the flow is supersaturated.

Two independent parameters of state (such as pressure and temperature) are updated at each time step using the Newton-Raphson method to determine the other properties of the gas and liquid phases. The solution algorithm is illustrated in Fig. 3.

The calculations are repeated until stationary conditions are achieved, i.e.:

$$\sum_{i=1}^{N} \frac{\left|P_i^{n+1} - P_i^{n}\right|}{P_i^{n}} < \varepsilon \tag{17}$$

where N is the total number of elements. At the n^{th} time step, the pressure at the center of the i^{th} element is denoted as P_i^n. Solution convergence is achieved when the residual falls below the criterion $\varepsilon = 10^{-6}$. The subsequent time step is determined by the following equation:

$$\Delta t = \left(\frac{\Delta x}{u_{max}}\right)\mathrm{CFL} \tag{18}$$

where the Courant number is assumed to be CFL $= 0.4$.

2.7. Initial and boundary conditions

The nozzle inlet conditions are defined by specified temperature and pressure. At the nozzle exit, conservative vectors ($\vec{Q}_N$) are determined through extrapolation from interior control volumes by using the formula $\vec{Q}_N = 2\vec{Q}_{N-1} - \vec{Q}_{N-2}$. Similarly, the inlet flow rate is also calculated via extrapolation of the second conservative component ($Q_0(2) = 2Q_1(2) - Q_2(2)$) and adjusted during the solution to reflect throat choking. Table 1 provides further details on the boundary conditions.

2.8. Principal assumptions

The main assumptions governing the model are summarized with their ranges of validity in Table 2.

3. Results

The following Section 3.1 presents the validation of the obtained results against available theoretical and experimental data for well-known nozzles. Therefore, the accuracy of the Peng-Robinson EOS in predicting the saturation compressibility and pressure of hydrogen is thus investigated. In the continuing, the pressure and equivalent droplet radius distributions resulting from 1D numerical modeling are compared against a performed 2D solution in ANSYS Fluent 19.1 and

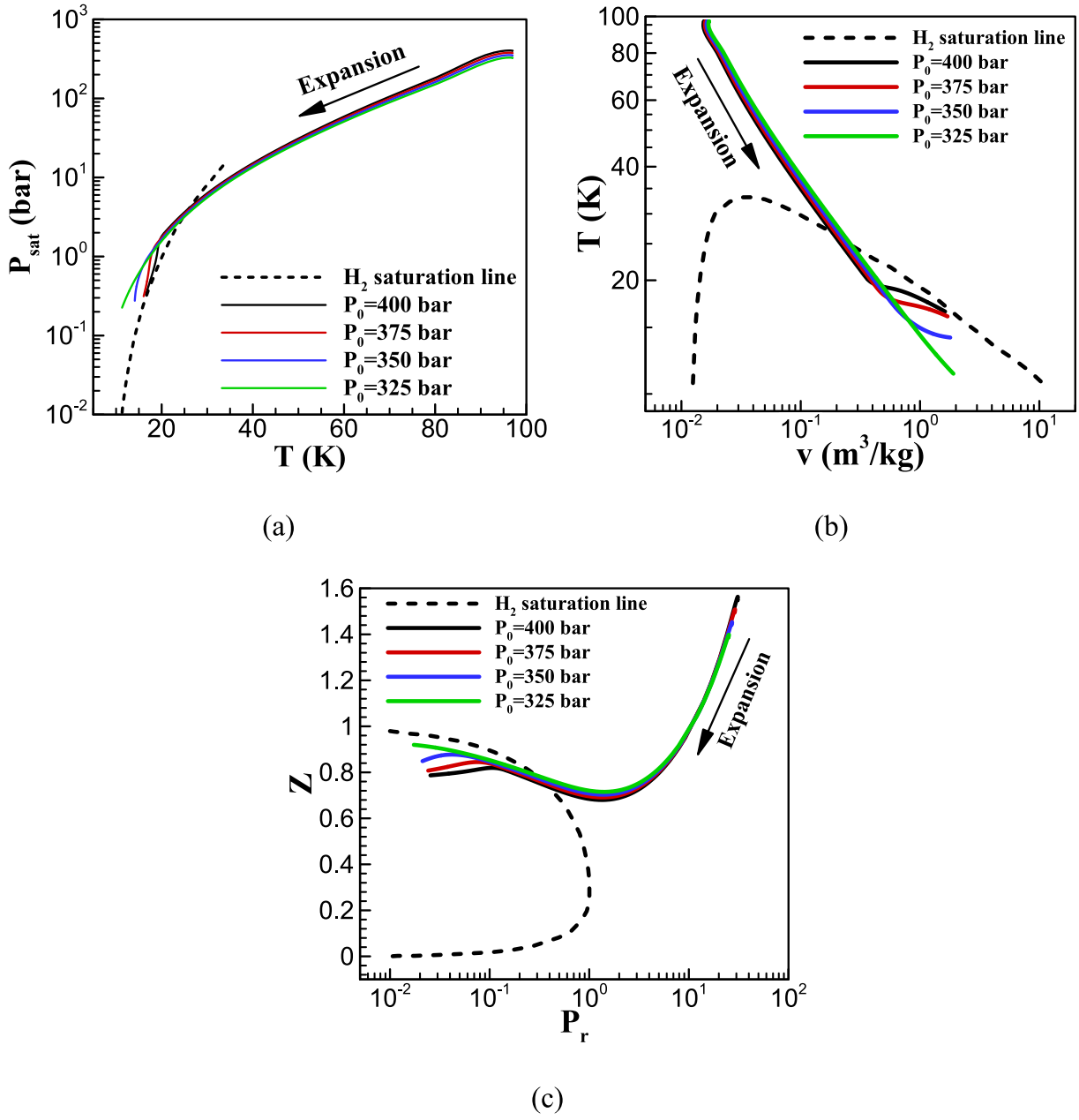

Fig. 7. Thermodynamic diagrams (*P-T*, *P-v*, and *Z-P*$_r$) for hydrogen liquefaction when inlet pressure ranges from 325 to 400 bar at the fixed inlet temperature of 97 K.

available experimental data for steam and non-steam expanding vapors. Furthermore, in Sections 3.2 and 3.3, the effects of inlet operational conditions (such as temperature and pressure) on the condensation and thermodynamic parameters of the nozzle are studied. For realistic inlet conditions, the inlet temperature is assumed to be around 100 K, with a pressure below 400 bar. Such inlet temperatures can be achieved by using precooling heat exchangers containing liquid nitrogen or using the cold flow from the nozzle in the precooling heat exchanger, while the high inlet pressures can be provided by advanced turbo-compressors with high-compression ratios. Through the analysis, it is assumed that the flow consists of pure hydrogen, free of impurities such as O_2, N_2, CO_2, and H_2O, whose frozen particles can form initial sites of partial heterogeneous condensation and flow obstructions.

3.1. Validating the results

Since there is no reliable data for the non-equilibrium condensation of hydrogen through experimental nozzles, the condensation and EOS models are validated here. Therefore, the compressibility factor and saturation pressure of hydrogen extracted from the EOS are compared with the saturation data available [73,74] (see Fig. 4). The *Z-Pr* saturation diagram data [73], valid for all simple fluids, has been derived by the Lee–Kesler EOS, which is an accurate model for describing the gas and liquid behavior accurately. As can be seen in Fig. 4a and b, the Peng-Robinson EOS predicts the gas and liquid saturation data accurately in a wide range of temperatures from the triple to the critical points of hydrogen. In addition, it can also be concluded that the condensation properties (e.g., liquid phase density) that are used in the calculations have enough accuracy in presenting hydrogen condensation behavior.

Figs. 5a–c consider the non-equilibrium condensation of steam in the Moore et al. [75] and IWSEP nozzles [76] to validate the 1D Eulerian solver and condensation models. First, the 2D contours of pressure and droplet equivalent radius, derived from the ANSYS Fluent 2D inviscid solution, are shown in Figs. 5a and b. Then, the average pressure and

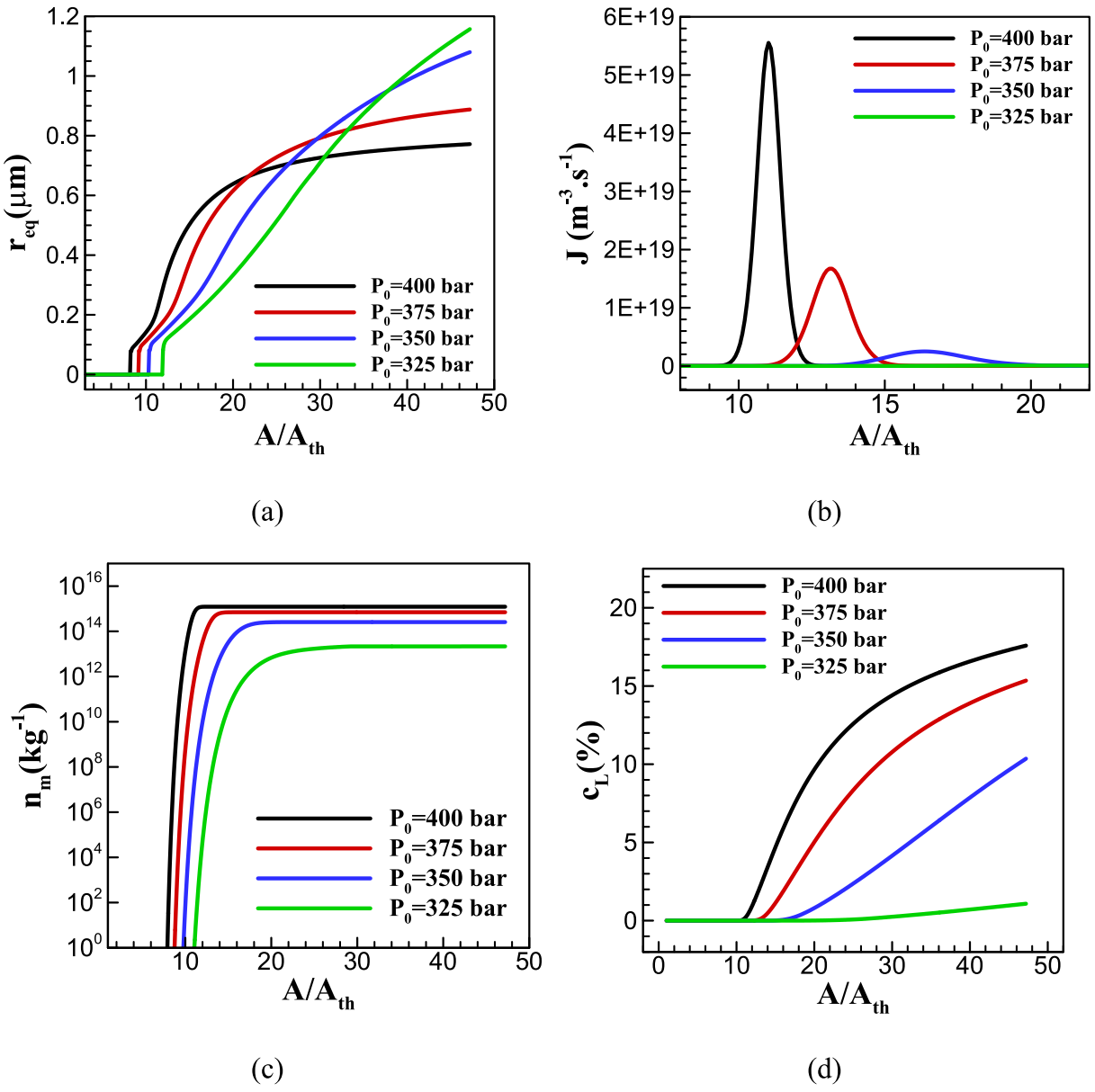

Fig. 8. Variation of droplet (a) radius, (b) nucleation rate, (c) number density, and (c) mass fraction in the nozzle for different inlet pressures when $T_0 = 97$ K.

droplet radius at each section of the divergent part from the ANSYS Fluent simulations are presented as a reference to validate the 1D modeling analysis. Furthermore, the pressure and droplet size are compared with the experimental data of Moore et al. [75]. The normalized mean absolute error of the 1D solution for determining the pressure and droplet size against the ANSYS Fluent numerical solution is about 8% and 47.5%, respectively. In addition, the normalized mean absolute error of the 1D analysis against the experimental data is about 7.6% for pressure and 26.5% for droplet size. Hence, it can be concluded that the proposed 1D model is sufficiently accurate for analyzing the non-equilibrium condensation of vapors in nozzles by predicting flow parameters and droplet size distributions. The difference between the ANSYS Fluent numerical and the 1D solution in predicting the experimental data is due to the difference in growth, EOS models, and property formulations used. For example, ANSYS Fluent uses the Young growth model and Virial EOS [60] to describe the vapor state. Additionally, sectional averaging of the pressure and droplet radius in the 2D solution are employed there to obtain distortion-free data in the x-direction through the nozzle.

Fig. 5d presents the pressure and droplet radius size distribution compared with the experimental data for the IWESP nozzle [76]. It can be seen that the 1D model provides an acceptable accuracy in the determination of pressure, condensation shock location, and strength. In addition, it is observed that droplet sizes resulting from 1D modeling are in the same range as experimental data [76]. Such errors can be attributed to the circumstance that the single-diameter 1D model does not consider the droplet size distribution in each section. Moreover, the Kantrowitz nucleation and growth models may also have some deficiencies within various pressure and temperature ranges, given that these models are derived via ideal gas assumptions [60]. The deviations (Figs. 5c and d) likely arise from model simplifications such as inviscid flow, stagnant nucleation, and neglecting phase slip and coalescence combined with uncertainties in experimental droplet size measurements.

To validate the models for predicting flow and condensation parameters of non-steam vapors, the numerical solution for CO_2 pressure distribution in the nozzle of Littieri et al. [77] and NH_3 Wilson points in the nozzle of Jaeger et al. [78] were compared (as shown in Figs. 6a and

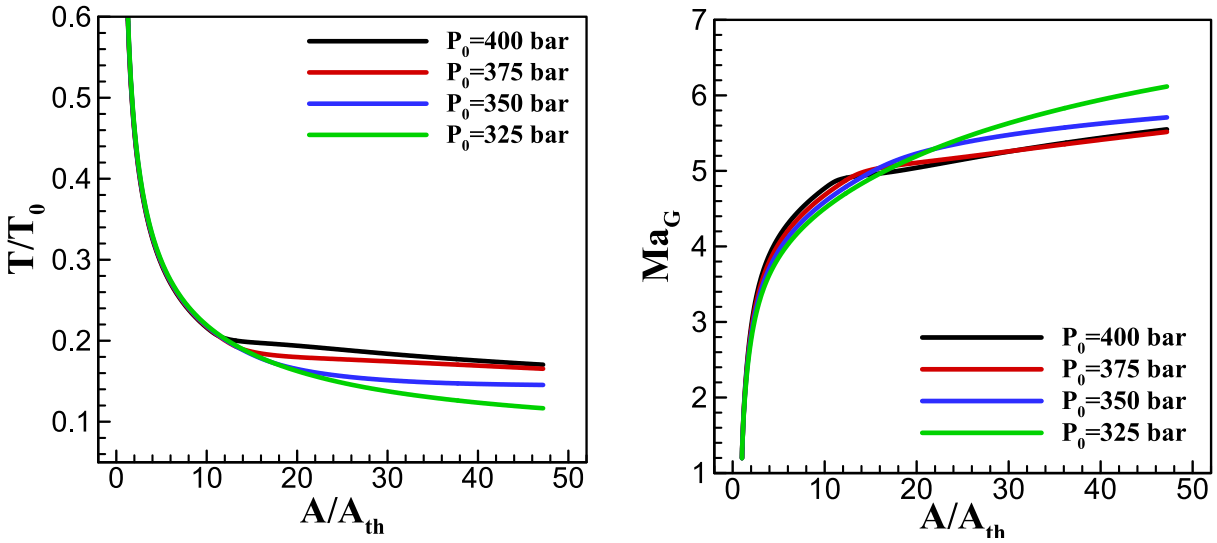

Fig. 9. Variation of (a) the flow temperature and (b) the Mach number in the nozzle for different inlet pressures when $T_0 = 97$ K.

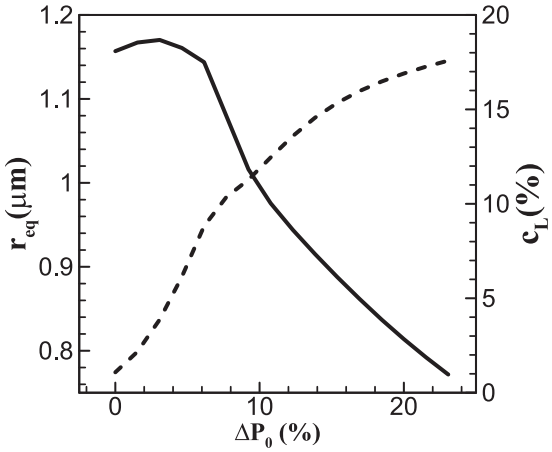

Fig. 10. Influence of the inlet pressure enhancement on the outflow droplet radius and liquefaction yield for $T_0 = 97$ K and $P_0 = 325$ bar.

b, respectively). The normalized mean absolute error of numerical solution against experimental data of Lettieri et al. [77] and Jaeger et al. [78] are 2.3% and 8.7%, respectively. Therefore, the current model is capable to be used for modeling H_2 condensation in nozzles. Usually, the Wilson points are approximately fixed, while the difference between the Wilson points derived from numerical solutions and experimental data is due to the difference between the divergent angle of the nozzle in the numerical solutions and the nozzle studied by Jaeger et al. [78].

3.2. Effects of inlet pressure

It was demonstrated in Section 3.1 that the presented 1D model has an adequate accuracy when calculating the two-phase parameters of various vapors, including H_2O, CO_2, and NH_3 in supersonic nozzles. Moreover, the droplet radius is one of the most sensitive parametrs in such problems. This means that the deviations in determining the submicron size of droplets are higher than deviations in pressure or liquid mass fraction distribution. Therefore, the model can successfully be used to predict the parameters of two-phase hydrogen flow (such as pressure, liquefaction yield, and even droplet size behavior) in Laval nozzles. Generating liquid hydrogen in supersonic nozzles necessitates low inlet temperatures and high pressures. The adiabatic expansion of hydrogen within the nozzle drives the gas to much lower temperatures and pressures. The nozzle specifications used in this study, assuming frictionless walls, are detailed in Appendix B.

Figs. 7a–c presents *P-T*, *P-v*, and *Z-P*$_r$ diagrams for inlet pressures of 325 to 400 bar at a constant temperature of 97 K. As can be seen, hydrogen gas starts to condense around $T = 20$ K and $P = 1.5$ bar in the nozzle. The diagrams illustrate that the increased inlet pressure reduces the supercooling temperature but enhances the overall non-equilibrium condensation within the nozzle due to the higher nucleation rate (see Figs. 7a, 8b and c). This intensified condensation releases more heat, resulting in a higher nozzle exit temperature. Consequently, the flow further deviates from the isentropic dry flow assumptions, thus approaching near-equilibrium or saturation conditions at the nozzle exit.

Fig. 7c demonstrates that the nozzle inlet flow deviates significantly from the isentropic dry gas behavior. During expansion in the convergent and divergent sections, the compressibility factor decreases. However, in the divergent section, it increases and initially tends to unite as the flow enters the two-phase region upon crossing the saturation line. Non-equilibrium condensation then stops this trend, causing the compressibility factor to decrease again, an effect intensified by higher inlet pressures.

Fig. 8 illustrates the distribution of droplet radius, nucleation rate, number density, and liquefaction yield within the nozzle for various inlet compression pressures with the maximum expansion of $A/A_e = 47.4$. As can be seen, due to the high heat capacity of hydrogen vapor, it has a significant capacity to absorb latent heat released during condensation without a large increase in the two-phase flow temperature. This allows for sustained higher supercooling during the expansion process, enabling the droplets to grow further, so that the droplet radius can exceed 1 μm. As a result, hydrogen has a high potential for liquefaction by the supersonic separation technique. Increasing inlet pressure leads to upstream condensation onset, higher nucleation rates, and smaller droplet sizes at the nozzle exit. However, the liquid phase mass fraction increases overall. After crossing the Wilson line and returning to quasi-equilibrium conditions, nucleation stops, and droplet growth slows due to reduced supercooling. Consequently, the rate of increase in liquid mass fraction diminishes, particularly at 400 bar, indicating limited liquefaction yield for each separation stage in the nozzle. The maximum liquid mass fraction achieved is 18%.

Fig. 9 depicts the temperature and Mach number distributions throughout the nozzle for different inlet pressures. Notably, achieving supersaturation states of hydrogen necessitates high area ratio nozzles, which generate hypersonic flow with a Mach number of $5.5 < \mathrm{Ma} < 6.5$

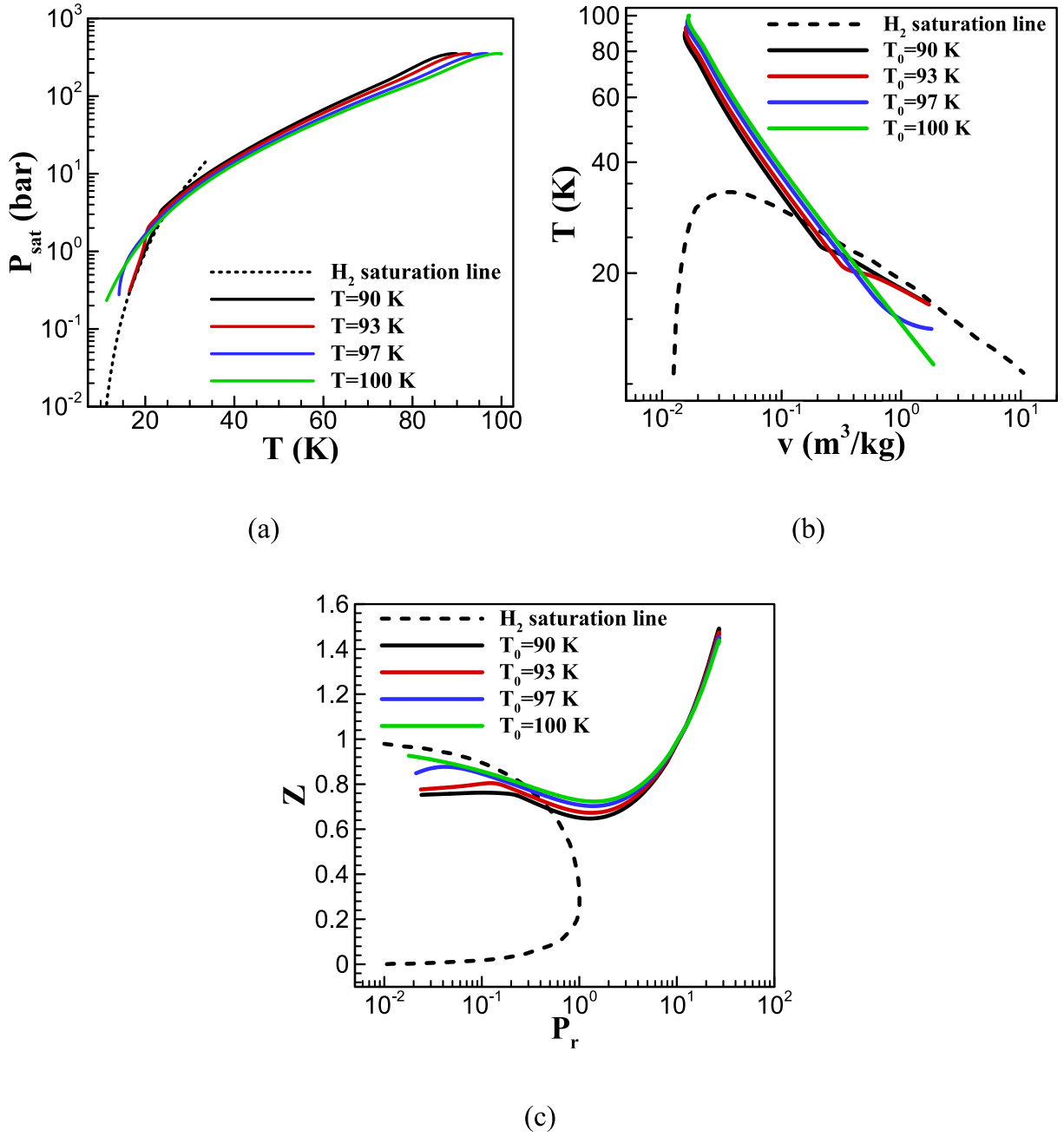

Fig. 11. Thermodynamic diagrams (*P-T, P-v,* and *Z-P*$_r$) for hydrogen liquefaction when the inlet temperature ranges from 90 to 100 K at a fixed inlet pressure of 350 bar.

at the outlet. The flow experiences a temperature drop as it progresses, reaching the Wilson point, the location of maximum supersaturation. Subsequently, the latent heat release causes a temperature rise, accompanied by a Mach number decrease as the gas and liquid phases reach equilibrium. In the post-equilibrium region, the Mach number increases again, though at a reduced rate (as compared with the dry flow), due to a slow increase of the liquid phase from droplet growth. For the case when $P_0 = 400$ bar, the condensation starts at $A/A_{th} = 12$ and at the nozzle exit, while the temperature difference between the condensing and dry flow scenarios is roughly 6 K. Increasing the inlet pressure moves the non-equilibrium condensation zone upstream, leading to a more pronounced condensation shock and a greater Mach number reduction in the droplet formation region.

Fig. 10 demonstrates the sensitivity of the droplet size and mass fraction at the nozzle outlet as affected by the inlet pressure, while keeping the inlet temperature constant. Due to the hydrogen's high specific heat capacity, increasing the inlet pressure leads to the formation of micron-sized droplets, optimizing liquefaction yield and simplifying droplet separation. This makes the supersonic separators an ideal choice for hydrogen liquefaction. As the inlet pressure rises, the droplet size decreases due to the decrease in Wilson point supercooling, while the liquid mass fraction increases. For a 23% compression pressure (relative to $P_0 = 325$ bar), the droplet radius is approximately 0.77 μm, while the liquid phase mass fraction is around 18%. However, for inlet pressure enhancements below 3%, the incomplete nucleation and the system's failure to achieve thermodynamic equilibrium led to a localized increase in the droplet size. Additionally, when pressure enhancements are below 10%, the outlet radius sizes exceed one micron.

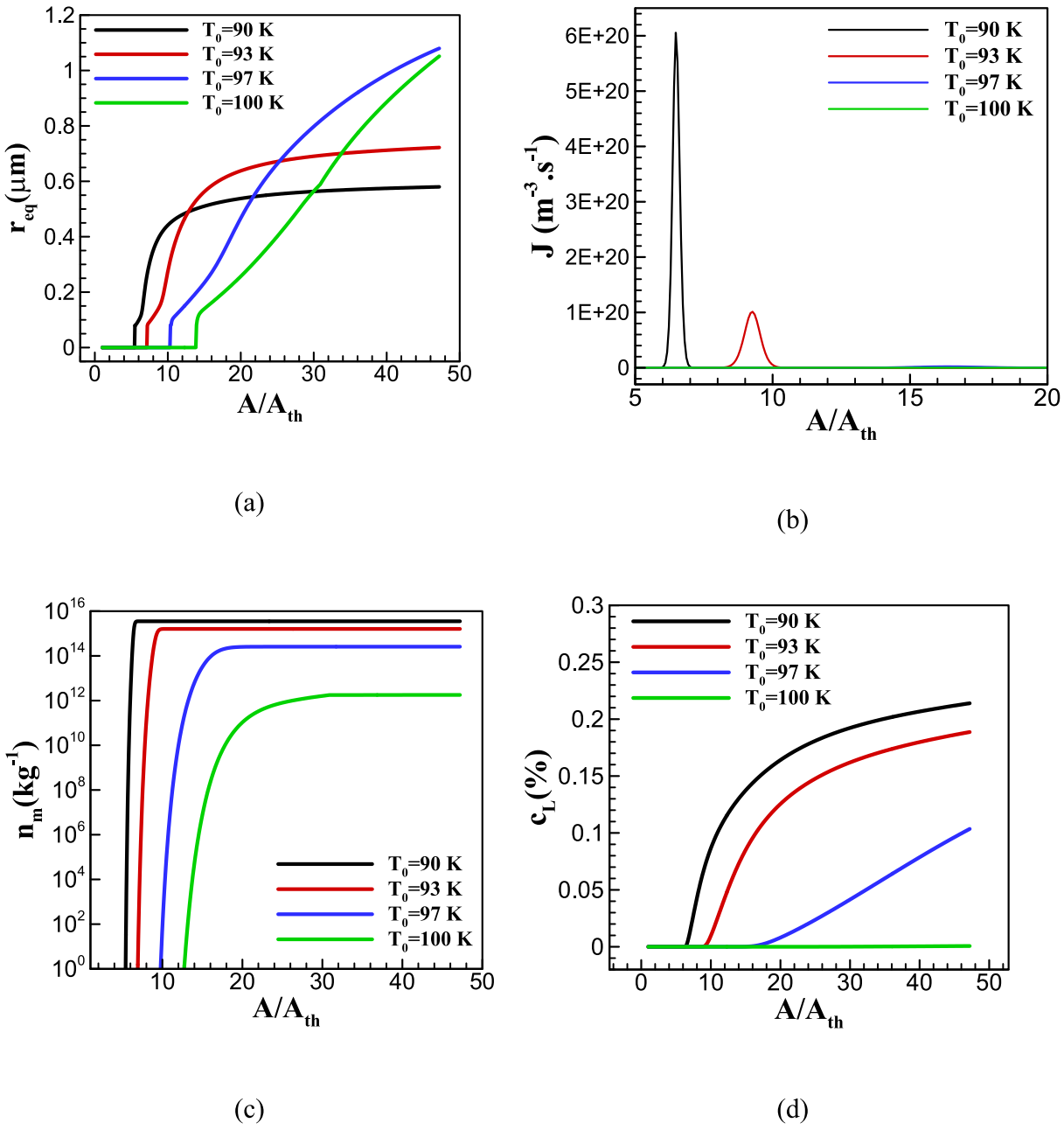

Fig. 12. Variation of droplet (a) equivalent diameter, (b) nucleation rate, (c) number density, and (d) liquefaction yield throughout the nozzle when the inlet temperature ranges from 90 to 100 K at a fixed inlet pressure of 350 bar.

3.3. Effects of inlet temperature

This section analyses the influence of inlet temperature on the thermodynamic and two-phase flow characteristics of a supersonic separator nozzle (operating at a fixed pressure of 350 bar). Fig. 11a-c demonstrates that decreasing the inlet temperature significantly decreases the Wilson point supercooling and enhances hydrogen liquefaction, thereby facilitating droplet gas-liquid equilibrium within the supersaturation region. In contrast, when the inlet temperature is 100 K or higher, the liquefaction potential is substantially reduced, leading to a low latent heat release and a negligible rise in flow temperature during condensation. According to Figs. 11b and c, after providing equilibrium conditions at the nozzle outlet, the specific volume of the gas will be close to the gas saturation state, and the compressibility factor reaches $Z = 0.68$.

Figs. 12a–d depict the distribution of condensation parameters along the nozzle divergent section for various inlet temperatures. It can be seen that hydrogen droplets are formed at nanoscale sizes; however, due to their rapid growth, their size reaches the micron scale at the nozzle outlet. Obviously, lowering the inlet temperature shifts the onset of condensation towards the upstream region of the nozzle at lower area ratios. Additionally, reduced inlet temperatures lead to increased nucleation rates (up to 6×10^{20} m^3. s^{-1}) and decreased droplet radii (down to 0.6 μm). The dominant effect of the droplet number density over the droplet growth results in a significant increase in liquefaction yield, reaching up to 22% with a decrease in the inlet temperature. The relatively small slope of the liquid mass fraction curve suggests that the maximum supersonic liquefaction yield per nozzle stage is limited to the range of 20–25%, which is still a substantial achievement. Notably, for inlet temperatures exceeding 100 K, despite the considerable droplet growth, the low number density of the formed droplets in the low supersaturated region before the Wilson point results in an approximately zero liquid mass

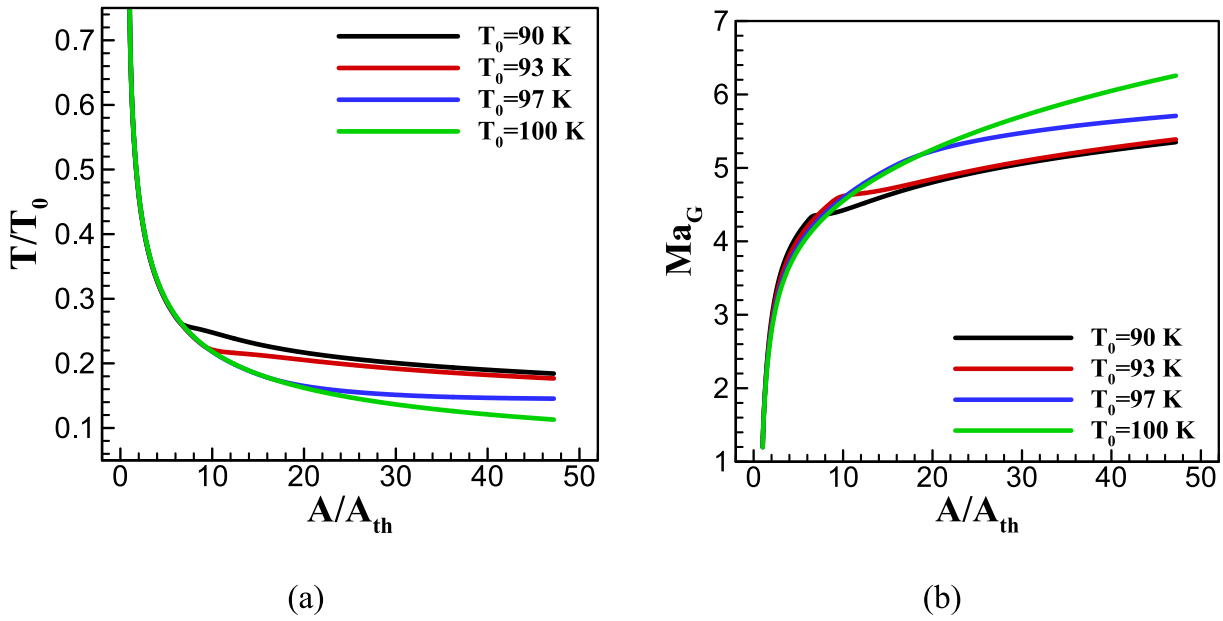

Fig. 13. Variation of (a) the flow temperature and (b) Mach number in the nozzle for different inlet temperatures when $P_0 = 350$ bar.

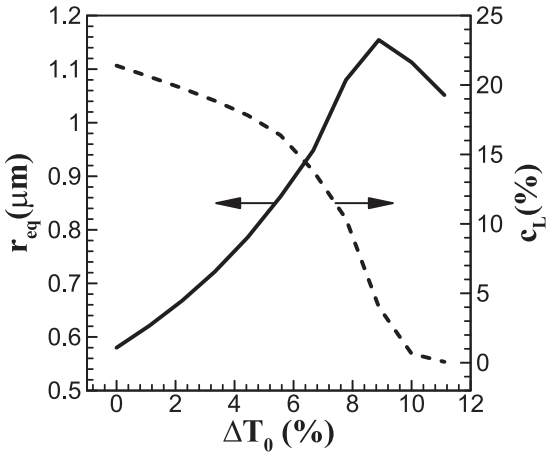

Fig. 14. The effects of inlet temperature on the outflow droplet radius and liquefaction yield for a fixed inlet pressure of $P_0 = 350$ bar ($T_0 = 90$ K).

fraction.

Figs. 13a and b illustrate the temperature and Mach number profiles along the nozzle for various area ratios, considering different inlet temperatures at a fixed inlet pressure. As the inlet temperature decreases, the onset of non-equilibrium condensation shifts upstream. For instance, in the case when $T_0 = 90$ K, the condensation initiates at $A/A_{th} = 6$, ending at a maximum temperature deviation of 12% relative to the isentropic flow at the nozzle exit (where the maximum reduction in Mach number as compared with the dry case reaches 1.4), which is a remarkable finding.

Fig. 14 demonstrates the sensitivity of droplet equivalent radius and the liquefaction yield at the nozzle outlet towards the inlet temperature, while keeping the inlet pressure at 350 bar. As can be seen, increasing the inlet temperature beyond 6% (relative to 90 K) leads to the formation of droplets with radii over one micron and reduces the liquefaction yield. As the inlet temperature rises, the droplet size increases, and the liquid mass fraction decreases. Therefore, for an inlet temperature of 90 K, the droplet radius is approximately 1.1 μm, and the liquid phase mass fraction is around 22%. For an inlet temperature increase over 9%, the incomplete nucleation and the system's inability to reach thermodynamic equilibrium before the Wilson point result in a local decrease in the outlet droplet radius trend. As is obvious from Figs. 10 and 14, the liquefaction and droplet growth of hydrogen are approximately twice as sensitive to the inlet temperature as to pressure (i.e., a decrease in the inlet temperature by 10% enhances the liquefaction yield by about 20%, while a 10% enhancement in the inlet pressure improves the liquefaction yield by some 10% only). On the other hand, a 10% reduction in temperature or a 10% enhancement in pressure results in a 50% and 20% reduction in droplet sizes, respectively. The physical reason for the condensation to be twice as sensitive to temperature as pressure is the increasing slope of the P-T saturation line with temperature. By increasing the inlet pressure, the isentropic expansion in the supersaturation region results in a shorter advancement in the supersaturation state than the similar process with a decrease in inlet temperature.

4. Concluding remarks

This study demonstrates the effectiveness of high-expansion Laval nozzles for industrial liquefaction of hydrogen as a suitable alternative to the J-T valves and the expansion devices in traditional cryogenic cycles. Generating a high amount of liquid hydrogen by means of non-equilibrium condensation is investigated numerically under realistic operating conditions and hypersonic nozzle flow. By employing a 1D CFD model (incorporating the Peng-Robinson equation of state and a modified Gyarmathy growth model based on the Clausius-Clapeyron relation), this study establishes that hydrogen's high heat capacity and low molecular mass enable substantial condensation and droplet growth beyond the Wilson point. In particular, a significant liquid-phase yield of 22% and the formation of micron-sized droplets can be achieved per separator nozzle stage. It has been shown that, due to the hypersonic flow velocity and low supercooling in the nozzle outlet, there is a liquefaction limitation for hydrogen in the separation applications. Due to the increase in the P-T saturation line slope with temperature, the inlet temperature is a more sensitive parameter as compared with the inlet pressure in terms of liquefaction yield and droplet size. This liquefaction yield is twice as sensitive to inlet temperature (A 10% reduction in inlet temperature results in a 20% increase in liquefaction yield, whereas a 10% increase in inlet pressure provides only a 10% gain). Furthermore, for cases with higher inlet temperatures and lower pressures, although the expansion to supersaturation states before the Wilson point results in micron-sized droplets, a negligible liquid mass

fraction is produced due to the low droplet number. Consequently, significant droplet growth requires inlet conditions that provide intense condensation, which occurs once the flow state crosses the Wilson point in the nozzle. The results also show that supersonic liquefaction reveals a promising avenue for reducing energy intensity and infrastructure demands in the cryogenic industry. Simultaneously, further research is still necessary with a focus on optimizing nozzle geometry and droplet management, with the ultimate goal to secure a scalable and sustainable hydrogen value chain for production, storage, and distribution.

CRediT authorship contribution statement

Masoud Sahami: Conceptualization, Data curation, Investigation, Methodology, Resources, Software, Writing – original draft. **Hojat Ghassemi:** Conceptualization, Formal analysis, Validation, Writing – review & editing. **Angel Terziev:** Conceptualization, Formal analysis, Supervision, Validation, Writing – review & editing. **Kostadin Fikiin:** Conceptualization, Formal analysis, Validation, Writing – review & editing. **Daniele Fiaschi:** Conceptualization, Formal analysis, Validation, Writing – review & editing. **George Pitchurov:** Conceptualization, Formal analysis, Writing – review & editing.

Declaration of competing interest

The authors declare that they have no known competing financial interests or personal relationships that could have appeared to influence the work reported in this paper.

Acknowledgments

M. Sahami would like to express his deep gratitude to the Technical University of Sofia for the opportunity to carry out a postdoctoral research fellowship.

This study is financed by the European Union – NextGenerationEU – through the National Recovery and Resilience Plan of the Republic of Bulgaria, Project No. BG-RRP-2.004-0005.

Appendix A. Relationships for the liquid and gaseous phases

Using existing data [74], a polynomial relationship between hydrogen saturation pressure and temperature is determined as follows:

$$P_s = a_0 + a_1 T + a_2 T^2 + a_3 T^3 + a_4 T^4 + a_5 T^5 + a_6 T^6 \quad (A.1)$$

where T and P_s are in Kelvin and bar, respectively. The coefficients a_0 to a_5 for various temperature ranges are presented in Table A.1.

Table A.1
Coefficients for calculation of the saturation pressure in Eq. (A.1).

	a_0	a_1	a_2	a_3	a_4	a_5	a_6
$T > 13.46$ K	8.009704322	−2.98687058	0.45046908	−0.0350771	0.00147456	−3.1278E-5	2.7023E-07
$T < 13.46$ K	−14,515.003	7079.4244	−1437.798	155.64214	−9.4713066	0.30720048	−0.004149

The density of liquid H_2 (in kg/m^3) is assumed to be a function of temperature, and it is correlated by Eq. A.2 [79]:

$$\rho_L = a_0 + a_1 T + a_2 T^2 + a_3 T^3 + a_4 T^4 + a_5 T^5 + a_6 T^6 \quad (A.2)$$

where T is in Kelvin. The coefficients a_0 to a_6 are presented in Table A.2.

Table A.2
Coefficients for calculating the density of liquid H_2 by Eq. (A.2).

a_0	a_1	a_2	a_3	a_4	a_5	a_6
−202.36155605	85.20761046	−10.502551	0.67676206	−0.0242709	4.59027417E-4	−3.587542E-6

Eq. (A.3), used to calculate the surface tension of H_2 droplets (in N/m), is derived by fitting data [80] as follows:

$$\sigma = a_0 + a_1 T + a_2 T^2 + a_3 T^3 + a_4 T^4 + a_5 T^5 \quad (A.3)$$

where T is in Kelvin. The coefficients a_0 to a_5 are presented in Table A.3.

Table A.3
Coefficients for calculating the surface tension of liquid H_2 by Eq. (A.3).

a_0	a_1	a_2	a_3	a_4	a_5
4.53873E-3	3.7227439E-5	−2.058324E-5	1.01021428E-6	−2.40912E-8	2.283444E-10

The latent heat of hydrogen (H_2) varies with temperature (in Kelvin) and can be determined by using Eq. (A.4) (in J/kg) [74,81]:

$$h_{fg} = a_0 + a_1 T + a_2 T^2 + a_3 T^3 + a_4 T^4 + a_5 T^5 + a_6 T^6 \quad (A4)$$

The coefficients a_0 to a_4 are presented in Table A.4.

Table A.4
Coefficients for calculating the latent heat by Eq. (A.4).

a_0	a_1	a_2	a_3	a_4	a_5	a_6
−86,712.735019	23,918.598124	−2695.733384	159.810158	−5.2588364	0.091135718	−6.50471E4

The gas specific enthalpy (h_G) is determined from the Peng-Robinson formulation as follows [82,83]:

$$h_G = \int_0^T C_{p0} dT + \left(\frac{T\frac{da}{dT} - a}{b\sqrt{8}} \right) \ln \left[\frac{1 + (1+\sqrt{2})b\rho_G}{1 + (1-\sqrt{2})b\rho_G} \right] \tag{A5}$$

where, C_{p0} represents the ideal gas isobaric specific heat capacity. The isochoric specific heat capacity for a real gas is calculated by Eq. (A.6) [82]:

$$C_v = \left(\frac{\partial u}{\partial T} \right)_v = C_{p0} - R + \left(\frac{T\frac{d^2a}{dT^2}}{b\sqrt{8}} \right) \ln \left[\frac{v_G + (1+\sqrt{2})b}{v_G + (1-\sqrt{2})b} \right] \tag{A6}$$

The Peng-Robinson equation's parameters, a and b, are used to compute the real gas isobaric specific heat capacity, according to Eq. (A.7) as specified in [84].

$$C_p = C_v - \left(\frac{Y^2}{X} \right) \left(\frac{Pv}{T} \right) \tag{A.7}$$

where $Y = T/P(\partial P/\partial T)_v$ and $X = -v/P(\partial P/\partial v)_T$. In the AUSM scheme, the flow Mach number for flux calculations is determined by:

$$\mathrm{Ma} = \frac{u}{\sqrt{\frac{\gamma P}{\rho_G}}} \tag{A.8}$$

where the real gas isentropic exponent is determined by Eq. (A.9):

$$\gamma = -\frac{v_G}{P} \left(\frac{\partial P}{\partial v_G} \right)_T \frac{C_p}{C_v} \tag{A.9}$$

The Chung method [85] is employed to accurately calculate the dynamic viscosity and thermal conductivity of the real gas across all pressure ranges.

$$\lambda_G(T,\ \rho_G) = \frac{31.2\mu_0\psi}{M} \left(G_2^{-1} + B_6\tilde{y} \right) + qB_7\tilde{y}^2 \sqrt{T_r} G_2 \tag{A.10}$$

$$\mu_G(T\rho_G) = \mu_G^* \frac{36.344\sqrt{m_1 T_c}}{v_c^{2/3}} \tag{A.11}$$

Eqs. (A.10) and (A.11) include the gas equivalent molecular mass (m_1) and critical temperature (T_c), with all other parameters (such as μ_0, ψ, G_2, $\tilde{y}$, etc.) derived as per a previously recommended methodology [85].

Appendix B. Nozzle profile

A quintic polynomial convergent nozzle, with a circular cross-section, is used in this investigation. The convergent profile is described by Eq. (B.1), and it is further detailed [34]:

$$R = R_{th} + (R_0 - R_{th}) \left[1 - 6\left(\frac{x}{L_c} \right)^5 + 15\left(\frac{x}{L_c} \right)^4 - 10\left(\frac{x}{L_c} \right)^3 \right] \tag{B.1}$$

The diverging part of the supersonic separator nozzle is designed within two distinct sections: A circular arc and a conical segment with a constant divergence angle. The nozzle's configuration and associated design parameters are detailed in Fig. B1 and Table B1.

Table B1
Coefficients related to the nozzle profile in Eq. (B.1) (α_d is the divergent angle, and R_r is the tangent circle radius at the nozzle throat in Fig. B1).

Parameter	R_i(mm)	R_{th} (mm)	R_r(mm)	L_C(mm)	R_e(mm)	α_D
Amount	60.33	7.54	147.03	211.16	51.9	1.5^0

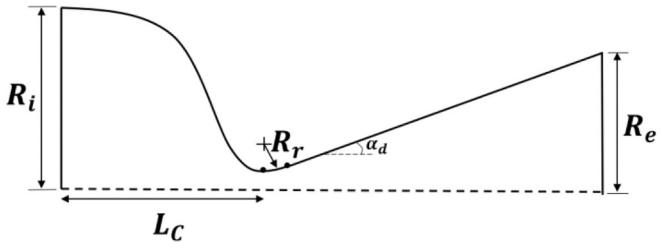

Fig. B1. Schematic of the design parameters corresponding to the studied nozzle.

Data availability

Details and clarifications could be obtained from the corresponding author upon request.

References

[1] Z. Xie, Q. Jin, G. Su, W. Lu, A review of hydrogen storage and transportation: progresses and challenges, Energies 17 (16) (2024) 4070, https://doi.org/10.3390/en17164070.

[2] A. Shabanpour-Haghighi, M. Karimaghaei, An overview on multi-carrier energy networks: from a concept to future trends and challenges, Int. J. Hydrogen Energy 47 (9) (2022) 6164–6186, https://doi.org/10.1016/j.ijhydene.2021.11.257.

[3] V.M. Avargani, S. Zendehboudi, N.M.C. Saady, M.B. Dusseault, A comprehensive review on hydrogen production and utilization in North America: prospects and challenges, Energ. Conver. Manage. 269 (2022) 115927, https://doi.org/10.1016/j.enconman.2022.115927.

[4] F. Veiga-López, D. Martínez-Ruiz, M. Kuznetsov, M. Sánchez-Sanz, Thermoacoustic analysis of lean premixed hydrogen flames in narrow vertical channels, Fuel 278 (2020) 118212, https://doi.org/10.1016/j.fuel.2020.118212.

[5] A. Alipour-Dehkordi, S.J. Neek, A. Shahnazar, Sustainable H2 production from glycerol steam reforming in the heat-integrated reactor: using reforming-side by-products as feed for the catalytic combustion-side, J. Ind. Eng. Chem. 113 (2022) 264–274, https://doi.org/10.1016/j.jiec.2022.05.054.

[6] B. Vivanco-Martín, A. Iranzo, Analysis of the European strategy for hydrogen: a comprehensive review, Energies 16 (9) (2023) 3866, https://doi.org/10.3390/en16093866.

[7] A. Galeev, Review of engineering solutions applicable in tests of liquid rocket engines and propulsion systems employing hydrogen as a fuel and relevant safety assurance aspects, Int. J. Hydrogen Energy 42 (39) (2017) 25037–25047, https://doi.org/10.1016/j.ijhydene.2017.06.242.

[8] J. Bian, X. Zhang, R. Zhang, W. Cai, Y. Hua, X. Cao, Conceptual design and analysis of a new hydrogen liquefaction process based on heat pump systems, Appl. Energy 374 (2024) 124020, https://doi.org/10.1016/j.fuel.2023.130401.

[9] M. Aziz, Liquid hydrogen: a review on liquefaction, storage, transportation, and safety, Energies 14 (18) (2021) 5917, https://doi.org/10.3390/en14185917.

[10] X. Duan, Z. Zhang, X. Cao, J. Bian, Supersonic expansion and condensation characteristics of hydrogen gas under different temperature conditions, Chin. J. Chem. Eng. 69 (2024) 220–226.

[11] E. Svendsmark, J. Straus, P.C. del Granado, Developing hydrogen energy hubs: the role of H2 prices, wind power and infrastructure investments in northern Norway, Appl. Energy 376 (2024) 124130, https://doi.org/10.1016/j.apenergy.2024.124130.

[12] P. Liu, T. Yang, T. Qiu, S. Ding, Thermodynamic analysis of power generation thermal management system for heat and cold exergy utilization from liquid hydrogen-fueled turbojet engine, Appl. Energy 365 (2024) 123290, https://doi.org/10.1016/j.apenergy.2024.123290.

[13] J. Dewar, Liquid hydrogen, Science 11 (278) (1900) 641–651, https://doi.org/10.1126/science.11.278.641.

[14] A. Züttel, Hydrogen storage methods, Naturwissenschaften 91 (2004) 157–172, https://doi.org/10.1007/s00114-004-0516-x.

[15] L. Yin, Y. Ju, Review on the design and optimization of hydrogen liquefaction processes, Front. Energy 14 (2020) 530–544, https://doi.org/10.1007/s11708-019-0657-4.

[16] T. Nandi, S. Sarangi, Performance and optimization of hydrogen liquefaction cycles, Int. J. Hydrogen Energy 18 (2) (1993) 131–139, https://doi.org/10.1016/0360-3199(93)90199-K.

[17] T. Numazawa, K. Kamiya, T. Utaki, K. Matsumoto, Magnetic refrigerator for hydrogen liquefaction, Cryogenics 62 (2014) 185–192, https://doi.org/10.1016/j.cryogenics.2014.03.016.

[18] M. Aasadnia, M. Mehrpooya, H. Ansarinasab, A 3E evaluation on the interaction between environmental impacts and costs in a hydrogen liquefier combined with absorption refrigeration systems, Appl. Therm. Eng. 159 (2019) 113798, https://doi.org/10.1016/j.applthermaleng.2019.113798.

[19] S. N. Shoghl, R. Nazerifard, and A. Naderifar, "Improvement of recovery of gaseous fluids using the replacement of supersonic separator instead of Joule–Thomson valve in dehydration/NGL recovery unit with computational fluid dynamic modeling," Chem. Eng. Res. Des., vol. 148, pp. 1–10, 2019, Doi: https://doi.org/10.1016/j.cherd.2019.05.029.

[20] W. Sun, S. Chen, Y. Hou, S. Bu, Numerical studies on two-phase flow in cryogenic radial-inflow turbo-expander using varying condensation models, Appl. Therm. Eng. 156 (2019) 168–177, https://doi.org/10.1016/j.applthermaleng.2019.04.047.

[21] S. Krasae-in, Efficient hydrogen liquefaction processes. http://hdl.handle.net/11250/235025, 2013.

[22] G. Peixer, J. Bordignon, T. Dias, Y. Sganzerla, J. Lozano, and J. Barbosa, "Comparison of conventional and emerging technologies for hydrogen liquefaction," in *Proceedings of the 26th IIR International Congress of Refrigeration. International Institute of Refrigeration, Paris, France*, 2023, Doi: 10.18462/iir.icr.2023.0868.

[23] A. F. Ismail, K. C. Khulbe, and T. Matsuura, "Gas separation membranes," Switz. Springer, vol. 10, pp. 973–978, 2015, Doi: https://doi.org/10.1007/978-3-319-01095-3.

[24] F. Rezaei, P. Webley, Optimum structured adsorbents for gas separation processes, Chem. Eng. Sci. 64 (24) (2009) 5182–5191, https://doi.org/10.1016/j.ces.2009.08.029.

[25] F. Zhao, Z. Wang, B. Dong, M. Li, Y. Ji, F. Han, Comprehensive life cycle cost analysis of ammonia-based hydrogen transportation scenarios for offshore wind energy utilization, J. Clean. Prod. 429 (2023) 139616, https://doi.org/10.1016/j.jclepro.2023.139616.

[26] M. Bampaou, K. Panopoulos, An overview of hydrogen valleys: current status, challenges and their role in increased renewable energy penetration, Renew. Sustain. Energy Rev. 207 (2025) 114923, https://doi.org/10.1016/j.rser.2024.114923.

[27] A. Riaz, M.A. Qyyum, S. Min, S. Lee, M. Lee, Performance improvement potential of harnessing LNG regasification for hydrogen liquefaction process: energy and exergy perspectives, Appl. Energy 301 (2021) 117471, https://doi.org/10.1016/j.apenergy.2021.117471.

[28] J. Yang, Y. Li, H. Tan, Integrated hydrogen liquefaction process with a dual-pressure organic Rankine cycle-assisted LNG regasification system: design, comparison, and analysis, Appl. Energy 347 (2023) 121372, https://doi.org/10.1016/j.apenergy.2023.121372.

[29] H. Ansarinasab, M. Fatimah, Y. Khojasteh-Salkuyeh, Conceptual design of two novel hydrogen liquefaction processes using a multistage active magnetic refrigeration system, Appl. Therm. Eng. 230 (2023) 120771, https://doi.org/10.1016/j.applthermaleng.2023.120771.

[30] J. Bian, J. Yang, Y. Li, Z. Chen, F. Liang, X. Cao, Thermodynamic and economic analysis of a novel hydrogen liquefaction process with LNG precooling and dual-pressure Brayton cycle, Energ. Conver. Manage. 250 (2021) 114904, https://doi.org/10.1016/j.enconman.2021.114904.

[31] W. Liu, L. Sun, L. Dong, T. Fujita, Trends and future challenges in hydrogen production and storage research, Environ. Sci. Pollut. Res. 27 (2020) 31092–31104, https://doi.org/10.1007/s11356-020-09470-0.

[32] V. Alfyorov, L. Bagirov, L. Dmitriev, V. Feygin, S. Imayev, J.R. Lacey, Supersonic nozzle efficiently separates natural gas components, Oil Gas J. 103 (20) (2005) 53–58.

[33] S. N. Shoghl, A. Naderifar, F. Farhadi, and G. Pazuki, "A novel strategy for process optimization of a natural gas liquid recovery unit by replacing Joule–Thomson valve with supersonic separator," Sci. Rep., vol. 12, no. 1, p. 22398, 2022, Doi: https://doi.org/10.1038/s41598-022-26692-z.

[34] X. Cao, J. Bian, Supersonic separation technology for natural gas processing: a review, Chemical Engineering and Processing-Process Intensification 136 (2019) 138–151, https://doi.org/10.1016/j.cep.2019.01.007.

[35] M. Malyshkina, The procedure for investigation of the efficiency of purification of natural gases in a supersonic separator, High Temp. 48 (2) (2010) 244–250, https://doi.org/10.1134/S0018151X10020161.

[36] Y. Yang, J.H. Walther, Y. Yan, C. Wen, CFD modeling of condensation process of water vapor in supersonic flows, Appl. Therm. Eng. 115 (2017) 1357–1362, https://doi.org/10.1016/j.applthermaleng.2017.01.047.

[37] V. Balepin, Supersonic Post-Combustion Inertial CO2 Extraction System Final Report, Alliant Techsystems Operations LLC, Ronkonkoma, NY (United States), 2017. https://www.netl.doe.gov/node/7096.

[38] J. Chen, A. Li, Z. Huang, W. Jiang, G. Xi, Non-equilibrium condensation in flue gas and migration trajectory of CO2 droplets in a supersonic separator, Energy 276 (2023) 127589, https://doi.org/10.1016/j.energy.2023.127589.
[39] J. Bian, Y. Liu, X. Zhang, Y. Li, L. Gong, X. Cao, Co-condensation and interaction mechanism of acidic gases in supersonic separator: a method for simultaneous removal of carbon dioxide and hydrogen sulfide from natural gas, Sep. Purif. Technol. 322 (2023) 124296, https://doi.org/10.1016/j.seppur.2023.124296.
[40] G. Zhang, X. Zhang, F. Wang, D. Wang, Z. Jin, Z. Zhou, Numerical investigation of novel dehumidification strategies in nuclear plant steam turbine based on the modified nucleation model, International Journal of Multiphase Flow 120 (2019) 103083, https://doi.org/10.1016/j.ijmultiphaseflow.2019.103083.
[41] Y. Liu, X. Cao, J. Yang, Y. Li, J. Bian, Energy separation and condensation effects in pressure energy recovery process of natural gas supersonic dehydration, Energ. Conver. Manage. 245 (2021) 114557, https://doi.org/10.1016/j.enconman.2021.114557.
[42] Y. Liu, X. Cao, D. Guo, H. Cao, J. Bian, Influence of shock wave/boundary layer interaction on condensation flow and energy recovery in supersonic nozzle, Energy 263 (2023) 125662, https://doi.org/10.1016/j.energy.2022.125662.
[43] M.A.F. Aliabadi, M. Bahiraei, Effect of water nano-droplet injection on steam ejector performance based on non-equilibrium spontaneous condensation: a droplet number study, Appl. Therm. Eng. 184 (2021) 116236, https://doi.org/10.1016/j.applthermaleng.2020.116236.
[44] A. Zou, Y. Zeng, E. Luo, New generation hydrogen liquefaction technology by transonic two-phase expander, Energy 272 (2023) 127150, https://doi.org/10.1016/j.energy.2023.127150.
[45] H. Ding, Y. Dong, Y. Zhang, Y. Yang, C. Wen, Energy efficiency assessment of hydrogen recirculation ejectors for proton exchange membrane fuel cell (PEMFC) system, Appl. Energy 346 (2023) 121357, https://doi.org/10.1016/j.apenergy.2023.121357.
[46] B. Chen, Y. Zeng, E. Luo, N. Peng, A. Zou, An innovative method for helium refrigeration liquefaction utilizing transonic nozzle, Energy 314 (2025) 134283, https://doi.org/10.1016/j.energy.2024.134283.
[47] K.K. Dingilian, R. Halonen, V. Tikkanen, B. Reischl, H. Vehkamäki, B.E. Wyslouzil, Homogeneous nucleation of carbon dioxide in supersonic nozzles I: experiments and classical theories, Phys. Chem. Chem. Phys. 22 (34) (2020) 19282–19298, https://doi.org/10.1039/D0CP02279A.
[48] S. Jinno, Y. Fukuda, H. Sakaki, A. Yogo, M. Kanasaki, K. Kondo, Mie scattering from submicron-sized CO2 clusters formed in a supersonic expansion of a gas mixture, Opt. Express 21 (18) (2013) 20656–20674, https://doi.org/10.1364/OE.21.020656.
[49] R. Secchi, G. Innocenti, D. Fiaschi, Supersonic swirling separator for natural gas heavy fractions extraction: 1D model with real gas EOS for preliminary design, J. Nat. Gas Sci. Eng. 34 (2016) 197–215, https://doi.org/10.1016/j.jngse.2016.06.061.
[50] P.H. Niknam, D. Fiaschi, H.R. Mortaheb, B. Mokhtarani, Numerical investigation of multiphase flow in supersonic separator considering inner body effect, Asia Pac. J. Chem. Eng. 14 (6) (2019) e2380, https://doi.org/10.1002/apj.2380.
[51] Y. Yang, X. Zhu, Y. Yan, H. Ding, C. Wen, Performance of supersonic steam ejectors considering the nonequilibrium condensation phenomenon for efficient energy utilisation, Appl. Energy 242 (2019) 157–167, https://doi.org/10.1016/j.apenergy.2019.03.023.
[52] J. Bian, X. Cao, W. Yang, X. Song, C. Xiang, S. Gao, Condensation characteristics of natural gas in the supersonic liquefaction process, Energy 168 (2019) 99–110, https://doi.org/10.1016/j.energy.2018.11.102.
[53] J. Bian, W. Jiang, D. Hou, Y. Liu, J. Yang, Condensation characteristics of CH4-CO2 mixture gas in a supersonic nozzle, Powder Technol. 329 (2018) 1–11, https://doi.org/10.1016/j.energy.2018.06.196.
[54] M.A.F. Aliabadi, M.S. Pour, A comprehensive investigation of volumetric heating effects on supersonic nozzle flow patterns and condensation shocks, considering non-equilibrium condensation and gas dynamics characteristics, Thermal Science and Engineering Progress (2025) 103331, https://doi.org/10.1016/j.tsep.2025.103331.
[55] A. Bolaños-Acosta, J. Restrepo, J. Simões-Moreira, Two semi-analytical approaches for solving condensation shocks in supersonic nozzle flows, International Journal of Heat and Mass Transfer 173 (2021) 121212, https://doi.org/10.1016/j.ijheatmasstransfer.2021.121212.
[56] P.H. Niknam, D. Fiaschi, H. Mortaheb, B. Mokhtarani, An improved formulation for speed of sound in two-phase systems and development of 1D model for supersonic nozzle, Fluid Phase Equilib. 446 (2017) 18–27, https://doi.org/10.1016/j.fluid.2017.05.013.
[57] F. Bakhtar, K. Zidi, Nucleation phenomena in flowing high-pressure steam part 2: theoretical analysis, Proceedings of the Institution of Mechanical Engineers, Part A: Journal of Power and Energy 204 (4) (1990) 233–242, https://doi.org/10.1243/PIME_PROC_1990_204_032_02.
[58] C. Li, P. Peng, D. Zhou, L. Wan, Research progress in LiBH4 for hydrogen storage: a review, Int. J. Hydrogen Energy 36 (22) (2011) 14512–14526, https://doi.org/10.1016/j.ijhydene.2011.08.030.
[59] D. W. HA, H. W. NOH, Y. M. SEO, T. H. KOO, and R. K. KO, "Study on validity of pre-cooling system for hydrogen gas using cryocooler part I: experimental investigation and theoretical analysis," Journal of Hydrogen and New Energy, vol. 34, no. 4, pp. 350–357, 2023, https://koreascience.kr/article/JAKO202325149099404.pdf.
[60] M. Sahami, H. Ghassemi, A. Terziev, G. Pitchurov, Homogeneous condensation in high-speed flows: a review on droplet nucleation and growth models, J. Braz. Soc. Mech. Sci. Eng. 47 (12) (2025) 1–43, https://doi.org/10.1007/s40430-025-05984-1.
[61] D.-Y. Peng, D.B. Robinson, A new two-constant equation of state, Ind. Eng. Chem. Fundam. 15 (1) (1976) 59–64, https://doi.org/10.5541/ijot.752567.
[62] R. Becker, W. Döring, Kinetische behandlung der keimbildung in übersättigten dämpfen, Ann. Phys. 416 (8) (1935) 719–752, https://doi.org/10.1002/andp.19354160806.
[63] A. Kantrowitz, Nucleation in very rapid vapor expansions, J. Chem. Phys. 19 (9) (1951) 1097–1100, https://doi.org/10.1063/1.1748482.
[64] L. Zhang, B. Li, G. Chen, Z. Yang, Numerical analysis method for intra-stage non-equilibrium two-phase condensing flow in wet steam turbine and its application, Int. J. Therm. Sci. 193 (2023) 108494, https://doi.org/10.1016/j.ijthermalsci.2023.108494.
[65] W. Sun, L. Niu, S. Chen, X. Sun, Y. Hou, Numerical investigation of nitrogen spontaneous condensation flow in cryogenic nozzles using varying nucleation theories, Cryogenics 68 (2015) 19–29, https://doi.org/10.1016/j.cryogenics.2015.01.010.
[66] F. Bakhtar, J.B. Young, A.J. White, D. Simpson, Classical nucleation theory and its application to condensing steam flow calculations, Proc. Inst. Mech. Eng. C J. Mech. Eng. Sci. 219 (12) (2005) 1315–1333, https://doi.org/10.1243/095440605X8379.
[67] G. Gyarmathy, Grundlagen einer theorie der nassdampfturbine, ETH Zurich (1962), https://doi.org/10.3929/ethz-a-000087803.
[68] Y. Zhang, B. Li, Comparative study of droplet growth models for non-equilibrium condensation with temperature-dependent thermophysical coupling, Int. J. Multiphase Flow (2025) 105451, https://doi.org/10.1016/j.ijmultiphaseflow.2025.105451.
[69] S. Shabani, M. Majkut, S. Dykas, E. Lakzian, G. Zhang, Evaluation of a new droplet growth model for small droplets in condensing steam flows, Energies 17 (5) (2024) 1135, https://doi.org/10.3390/en17051135.
[70] A.J. Amaya, B.E. Wyslouzil, Ice nucleation rates near~ 225 K, J. Chem. Phys. 148 (8) (2018), https://doi.org/10.1063/1.5019362.
[71] J. Young, The condensation and evaporation of liquid droplets at arbitrary Knudsen number in the presence of an inert gas, Int. J. Heat Mass Transf. 36 (11) (1993) 2941–2956, https://doi.org/10.1016/0017-9310(93)90112-J.
[72] M.-S. Liou, A sequel to ausm: Ausm+, J. Comput. Phys. 129 (2) (1996) 364–382, https://doi.org/10.1006/jcph.1996.0256.
[73] R.E. Sonntag, C. Borgnakke, G.J. Van Wylen, S. Van Wyk, Fundamentals of Thermodynamics, Wiley, New York, 1998.
[74] J. Choi, "KAERI/TR-2723/2004 : Liquid Hydrogen Properties," 2004, https://www.osti.gov/etdeweb/servlets/purl/20599211.
[75] M. Moore, "Predicting the Fog-Drop Size in Wet-Steam Turbines," Presented at the Wet Steam 4th Conference, University of Warwick, 1973. https://cir.nii.ac.jp/crid/1574231874929479936.
[76] G. Zhang, S. Dykas, M. Majkut, K. Smołka, X. Cai, Experimental and numerical research on the effect of the inlet steam superheat degree on the spontaneous condensation in the IWSEP nozzle, Int. J. Heat Mass Transf. 165 (2021) 120654, https://doi.org/10.1016/j.ijheatmasstransfer.2020.120654.
[77] C. Lettieri, D. Paxson, Z. Spakovszky, P. Bryanston-Cross, Characterization of nonequilibrium condensation of supercritical carbon dioxide in a de Laval nozzle, J. Eng. Gas Turbines Power 140 (4) (2018) 041701, https://doi.org/10.1115/1.4038082.
[78] H.L. Jaeger, E.J. Willson, P.G. Hill, K.C. Russell, Nucleation of supersaturated vapors in nozzles. I. H2O and NH3, J. Chem. Phys. 51 (12) (1969) 5380–5388, https://doi.org/10.1063/1.1671959.
[79] J.W. Dean, A Tabulation of the Thermodynamic Properties of Normal Hydrogen from Low Temperatures to 5400 and from 10 to 1500 Psia; Supplement a (British Units), US Department of Commerce, National Bureau of Standards, 1962, https://doi.org/10.6028/NBS.TN.120A.
[80] A. Mulero, I. Cachadina, M. Parra, Recommended correlations for the surface tension of common fluids, J. Phys. Chem. Ref. Data Monogr. 41 (4) (2012), https://doi.org/10.1063/1.4768782.
[81] T. Flynn, Cryogenic engineering, revised and expanded, CRC Press (2004), https://doi.org/10.1201/9780203026991.
[82] S. Martynov, S. Brown, H. Mahgerefteh, An extended Peng-Robinson equation of state for carbon dioxide solid-vapor equilibrium, Greenhouse Gases: Sci. Technol. 3 (2) (2013) 136–147, https://doi.org/10.1002/ghg.1322.
[83] B. J. McBride, Coefficients for Calculating Thermodynamic and Transport Properties of Individual Species. National Aeronautics and Space Administration, Office of Management, Scientific and Technical Information Program, 1993, Doi: https://doi.org/10.1016/S0378-3812(00)00384-8.
[84] Y.A. Cengel, M.A. Boles, M. Kanoğlu, Thermodynamics: An Engineering Approach, McGraw-hill New York, 2011. https://www.arma.org.au/wp-content/uploads/2017/03/thermodynamics-an-engineering-approach-cengel-boles.pdf.
[85] B.E. Poling, J.M. Prausnitz, J.P. O'connell, Properties of Gases and Liquids, McGraw-Hill Education, 2001. https://www.accessengineeringlibrary.com/content/book/9780070116825.